Full Length Article

Experimental and theoretical insight into DSSCs mechanism influenced by different doping metal ions

Aleksandra Bartkowiak [a,b,*], Oleksandr Korolevych [c], Gian Luca Chiarello [b], Malgorzata Makowska-Janusik [c], Maciej Zalas [a]

[a] Faculty of Chemistry, Adam Mickiewicz University, Poznań, Uniwersytetu Poznańskiego 8, 61-614 Poznań, Poland
[b] Department of Chemistry, University of Milan, Via Golgi 19, 20133 Milano, Italy
[c] Faculty of Science and Technology, Jan Dlugosz University, Al. Armii Krajowej 13/15, 42-200 Czestochowa, Poland

ARTICLE INFO

ABSTRACT

Mesoporous TiO$_2$ doped with Cu^{2+}, Mn^{2+}, and Ni^{2+} ions nanomaterials with 0.4% content of dopant ions were synthesized *via* the optimized sol-gel method. Experimental results were compared with an extensive theoretical study of doped-TiO$_2$ nanoparticles using density functional theory extended by Hubbard correction. Structural analyses performed indicate anatase structure (with minor impurity of brookite) of spherical-shaped nanoparticles with a size below 15 nm. Further, XPS and EPR analyses confirmed the doping of metal ions into TiO$_2$ and the formation of oxygen vacancies. The characteristic narrowing of the energy bandgap was observed with a higher concentration of dopants than 0.4%. Nanomaterials were used to fabricate solar cells sensitized with N3 dye. Comprehensive analysis of photovoltaic results combined with theoretical calculations has been provided to propose a working principle mechanism of electron transport in the investigated nanomaterials. Each metal ion used during the nanomaterials' synthesis caused a different effect on the DSSC performance resulting from the structure of their energy bandgap. TiO$_2$ doped with Cu^{2+} and Mn^{2+} indicates a remarkable decrease in conductivity instead of TiO$_2$:Ni^{2+}. Therefore, the most effective nanomaterial for DSSC application turned out to be TiO$_2$:0.4 %Ni^{2+} with a photoconversion efficiency improvement compared to standard P25 titania.

1. Introduction

In the pursuit of a better eco-world, where human beings' existence depends on increasing the accent on taking care of our planet, the renewable energy source gains a great potential. Solar energy attracts great attention among different sustainable sources due to its silent, abundant, and environmentally friendly power [1]. Although silicon-based photovoltaic technology is still dominating the global market, researchers are looking for other solutions unceasingly [2]. One of them is dye-sensitized solar cells (DSSCs) – photovoltaic systems whose most promising application is highly efficient powering the wireless devices using indoor light in line with the Internet of Things concept [3]. Moreover, low-cost manufacturing and the possibility of forming thin and flexible solar systems increase their meaning from the economic perspective [4].

The DSSCs consist of photoanode (semiconductor with adsorbed dye molecules), counter electrode (thin layer of redox catalyst), and electrolyte in the interelectrode space (made of organic solvent with redox mediator) [5]. Briefly, dye molecules after absorption of a photon are excited from the ground state to the higher electron state. Then, an electron is injected into the semiconductor's conduction band (CB) and transported through an external circuit to the counter electrode. Meanwhile, the oxidized dye is regenerated by a redox mediator. Finally, the donated electron from the working electrode reduces the redox species. The whole cycle is closed and then repeated as long as illumination occurs. As can be seen, many processes belong to the photoconversion mechanism, and hence, every DSSC component is crucial for its proper working. However, particular attention should be paid to the semiconductor/dye interface present in the working electrode. Photoanode is usually made by a thin layer of binary or ternary metal oxides, such as TiO$_2$, ZnO, CeO$_2$, Al$_2$O$_3$, SrTiO$_3$, and Zn$_2$SnO$_4$ [6–11]. Among the compounds mentioned above, titanium dioxide (TiO$_2$) is the most commonly used material for the production of photoelectrodes [12]. It results from, among others, relatively small toxicity, chemical stability, and large specific surface area (providing better contact with a higher amount of dye molecules) [13]. Moreover,

---

due to the bandgap value of 3.20–3.22 eV, the TiO_2 shows an improved electron injection rate and low charge recombination, which directly influences the photoelectrochemical properties of DSSCs [14].

Even if TiO_2 occurs naturally in three kinds of polymorphs: anatase, rutile, and brookite (and the higher number obtained synthetically), the first one is the most favorable for DSSC application [15,16]. Park and co-workers justified that the short-circuit photocurrent of an anatase-based DSSC indicates about 30% higher value than in the rutile-based cells, which stems from the fact that electron transport rate is slower in the latter being [17]. The brookite structure is considered to be challenging to obtain synthetically [18]. What is more, similar to rutile, brookite indicates non-effective electron conduction between titania nano-particles that decreases DSSC's photoconversion efficiency [19]. Although anatase stands out from the other structures, it is not flawless. Due to the high energy bandgap and low thermal stability at higher temperatures (phase transformation to rutile), researchers are still looking for new solutions to modify TiO_2 to improve its electronic and structural properties [20]. There are three commonly known strategies to change TiO_2 properties: bandgap's narrowing, oxygen vacancy formation, or introduction of impurity energy levels [21]. Generally, it can be obtained by size-controlled syntheses or incorporation into TiO_2 crystal lattice dopants like metal and nonmetal ions [22]. Kumaravel et al. show that oxygen vacancies are formed after doping Mo^{6+} ions into TiO_2 [23]. It causes a reduction of Ti^{4+} and Mo^{6+} ions, which leads to the creation of additional energy levels in the bandgap above the valence band (VB) and improves photocatalytic activity [23]. On the other hand, Bramhankar and co-workers prepared co-doped TiO_2 with Ni^{2+} and Zn^{2+} ions and optimized their concentration to enhance electron injection efficiency by narrowing energy bandgaps and lowering the CB edge [24]. As can be seen, proper bandgap engineering can introduce relevant changes in the DSSC's working mechanism.

An insight at the atomic level is needed to explain the energy bands arrangement of the doped TiO_2 and predict the role of ions and structural changes in their electronic properties. That can be obtained by introducing quantum chemical calculations into a used methodology to study the properties of semiconducting materials. Compared to experimental reference data, the first level calculations analyzed can explain the intramolecular charge transfer occurring at the photoactivated surface of dye and doped semiconductors. Therefore, we present a holistic approach to investigating TiO_2 nanomaterials doped with d-block metal ions (Cu^{2+}, Mn^{2+}, Ni^{2+}) in a theoretical and experimental way.

2. Materials and methods

2.1. Computer simulations

In the presented work, computer simulations based on the first principle calculations studied the electronic properties of defected structures of TiO_2 in anatase form. The mentioned structures were based on supercells built of $2 \times 2 \times 1$ TiO_2 anatase crystal (α-TiO_2) unit cells. One Ti atom was substituted by one M = Ni, Mn, or Cu metal atom in each supercell, making the $M_{0.06}Ti_{0.94}O_2$ structure. The oxygen vacancy v(O) was also created in the metal-doped structures.

Structural and electronic properties were performed for the studied atomic structures using the Vienna ab initio simulation package (VASP) in version vasp.5.4.4 (VASP Software GmbH, Vienna, Austria) [25–27]. Electron structures of all atoms were described by sw-GW basis sets. The quantum chemical calculations were performed with generalized gradient approximation (GGA) applied to the density functional theory (DFT/GGA) method [28]. The Hubbard correction was used to avoid problems occurring with a description of the $3d$ electrons localized on transition metal atoms [29]. In this case, the rotation-invariant LSDA + U method introduced by Liechtenstein et al. was used [30]. The U and J parameters representing Coulomb interaction energy and exchange energy, respectively, were specified separately.

In quantum chemical calculations, the Hubbard correction was used only for 3d electrons of Ti, Ni, Mn, and Cu atoms. The J parameter was fixed as 1.0 eV for all atoms to optimize the geometry of all crystal structures. During the geometry optimization procedure, the Coulomb interaction energy parameter for the Ti atom was specified as $U_{Ti} = 6.0$ eV, for Mn, Cu, and Ni atoms: $U_{Mn} = 8.0$ eV, $U_{Cu} = 7.0$ eV, and $U_{Ni} = 6.0$ eV were selected, respectively [31–36]. The geometry optimization searching was performed, allowing full relaxation. The positions of atoms and lattice parameters were relaxed by applying the conjugate gradient method. A plane basis set was expanded in energy cut-off equal to 520 eV, and k point sampling was generated by the Monkhorst and Pack scheme with a mesh of point $8 \times 8 \times 8$ [37]. The total energy calculation over the Brillouin zone was made using the linear tetrahedron method with Bloch correction [38–40].

Electronic properties of the studied crystals were calculated following a simple path in the Brillouin zone depicted as Γ-F-Q-Z- Γ where F (0.0; 0.5; 0.0) and Q (0.0; 0.5; 0.5). The spin-polarized calculation with Fermi smearing was performed. Computations were augmented by Hubbard correction applying $U_{Ti} = 9.25$ eV and $U_{Mn} = 7.00$ eV [31,32,41]. In the case of Ni and Cu atoms, the Hubbard parameters for energy band calculations were the same as those described above and used for a geometry relaxation, i.e., $U_{Ni} = 6$ eV and $U_{Cu} = 7$ eV [42,43]. The J parameter was equal to 1 eV for all atoms.

The electrical conductivity for each studied doped-TiO_2 structure was calculated using BoltzTrap code, i.e., solving the semi-classic Boltzmann transport equation with the constant relaxation time (τ_R) approximation [44].

2.2. Materials

Titanium(IV) isopropoxide (TTIP, 97%), titanium(IV) chloride (99.9%), N3 dye (95% NMR), α-terpineol (96%), ethylcellulose (p.a.), iodine, 1-propyl-3-methyl-imidazolium iodide, guanidine thiocyanate, and 4-*tert*-butylpiridine were obtained from Sigma Aldrich (St. Louis, MO, USA). Acetic acid, nitric acid, anhydrous ethanol, ammonia water solution (25%), acetonitrile, copper(II), and manganese(II) nitrates of an analytical grade were obtained from POCh (Gliwice, Poland). Other chemical reagents, such as nickel(II) nitrate ($\geq$97%), isopropanol (i-PrOH, 99.8%), acetone (p.a.), and chloroplatinic acid (99.9%), were purchased from Fluka (Buchs, Switzerland), WITKO (Łódź, Poland), PPH Stanlab, (Lublin, Poland), and Merck (Darmstadt, Germany), respectively. During the whole experiment, demineralized water prepared in our lab was used. Reference titanium dioxide nanopowder was P25 Aeroxide (Evonik Industries AG, Essen, Germany). Transparent conductive glass (TCO) and ionomeric foil, such as fluorinated tin oxide glass (FTO) and Meltonic, were obtained from 3D nano (Kraków, Poland) and Solaronix (Aubonne, Switzerland), respectively.

2.3. Synthesis of TiO_2:Cu^{2+}/Mn^{2+}/Ni^{2+}

The TiO_2:M^{2+} (M = Cu^{2+}, Mn^{2+}, Ni^{2+}) nanomaterials were synthesized using the modified sol–gel method [32]. Typically, 0.592 mL of TTIP was added into 200 mL of i-PrOH and stirred vigorously for 15 min. Then, a 10 mM solution of acetic acid in i-PrOH was added dropwise for additional 40 min. During this time, aqua solutions of metal nitrates were prepared with a total volume of 30 mL. Details on the amount of added precursor, XRF results (percentage contribution of metal ions in TiO_2 nanomaterials), and labels of samples prepared in this work are available in Table 1. The concentration of metal nitrates was optimized to obtain a 0.4% amount of dopant ions into TiO_2 matrices. Therefore, nanomaterials with 0.4% content of M^{2+} ions were named TiO_2:M (M = Ni, Cu, Mn), and the others were labeled M−1 and M−2, corresponding to the increasing concentration of dopant ions. The solutions mentioned above were injected into the as-prepared mixture of TTIP and acetic acid in i-PrOH using a syringe pump with a 0.5 mL/min rate. Subsequently, 0.4 mL of nitric acid was introduced, turning the solution cloudy. After heating under reflux conditions for 75 min, an additional portion of

Table 1
Description of samples corresponding to the amount of added precursor and XRF results.

Nanomaterials' labels (series)	Nanomaterials' labels	Working electrodes' labels	Amount of added precursor [mol]	M^{2+} [%]
$TiO_2:Cu^{2+}$	$TiO_2:Cu$	$TiO_2:Cu\_FTO$	$2.02 \cdot 10^{-5}$	0.421
	Cu-1	Cu-1_FTO	$6.19 \cdot 10^{-5}$	1.348
	Cu-2	Cu-2_FTO	$1.00 \cdot 10^{-4}$	3.457
$TiO_2:Mn^{2+}$	$TiO_2:Mn$	$TiO_2:Mn\_FTO$	$2.02 \cdot 10^{-5}$	0.398
	Mn-1	Mn-1_FTO	$6.19 \cdot 10^{-5}$	0.509
	Mn-2	Mn-2_FTO	$1.00 \cdot 10^{-4}$	1.301
$TiO_2:Ni^{2+}$	Ni-1	Ni-1_FTO	$2.02 \cdot 10^{-5}$	0.124
	$TiO_2:Ni$	$TiO_2:Ni\_FTO$	$6.19 \cdot 10^{-5}$	0.377
	Ni-2	Ni-2_FTO	$1.00 \cdot 10^{-4}$	0.563

deionized water (7 mL) was added, and finally, after refluxing the mixture for 24 h, precipitates were filtered under reduced pressure. As-obtained samples were dried overnight at 60°C. Then, as-obtained materials were divided into two parts, where the first one was used to prepare a viscous paste and for analyses. The second part was annealed at 450°C for 2 h (7.5°C/min) and intended for further research.

2.4. Preparation of DSSC components and cells assembling

Viscous pastes based on previously prepared samples were done keeping the following ratio of the ingredients: 3 g of doped $TiO_2:M^{2+}$ material, 1 mL of acetic acid, and 20 mL of ethanol which formed mixture A and was held in an ultrasound bath for 3 h. Meanwhile, solution B was prepared by mixing: 10 mL of α-terpineol, 1.5 g of ethyl-cellulose, and 13.5 g of ethanol. When the solution B was added into the solution A, the as-obtained mixture was ultrasonicated for an additional hour and then vigorously stirred overnight [45]. After removing excess ethanol, titania pastes were deposited on previously cleaned FTO glasses (1:1 v/v, ethanol, and acetone mixture – 30 min in an ultrasonic bath) using the "doctor blade" method and annealed at 450°C for 2 h with a ramp rate of 7.5°C/min. As-prepared photoanodes were immersed in a 40 mM $TiCl_4$ aqueous solution and heated to 70°C for 1 h to form a protective, dispersive layer on TiO_2 coatings. Then, electrodes were washed with deionized water followed by ethanol, dried, and annealed at 450°C (ramp rate 7.5°C/min) for 30 min. An ethanolic N3 dye solution (10^{-4} M) was employed to sensitize the titania electrodes. Typically, the active area of as-prepared photoanodes was approximately 0.125 cm^2. Counter electrodes with a Pt layer were prepared by wiping the FTO glasses with a tissue soaked in the H_2PtCl_6 solution (23 g/L of Pt in ethanol) and subsequently calcined at 450°C for 30 min [46]. Finally, both electrodes were combined with an ionomeric foil (25 μm thick) sealant. The interelectrode space was filled with an electrolyte (acetonitrile solution consisting of 0.03 M iodine, 0.6 M 1-propyl-3-methyl-imidazolium iodide, 0.1 M guanidine thiocyanate, and 0.5 M 4-*tert*-butylpiridine), injected through the holes predrilled in the counter electrodes.

2.5. Dye loading determination

Working electrodes with around 3 cm^2 titania layer sensitized with N3 were prepared according to the above procedure to determine the amount of adsorbed dye molecules. Every photoanode was immersed for 30 min in the 2 M ammonia solution in ethanol. Subsequently, the desorbed dye solution was investigated using ultraviolet–visible (UV–vis) spectroscopy at 310 nm based on the calibration curve. Five photoelectrodes were prepared with every material synthesized in this work to obtain reliable results, and measurement results were averaged.

2.6. Characterization of materials and instrumentation

The crystal structure of as-obtained materials was analyzed by X-ray powder diffraction (XRD) measurement using a D8 Advance diffractometer (Bruker, Billerica, MA, USA) with Cu Kα (λ = 0.15406 nm). The concentration of metal ions was determined by X-ray fluorescence spectroscopy (XRF) on MiniPal2 equipment (PANalytical B.V., Almelo, The Netherlands). The calibration curves were done by mixing metal oxides (CuO, MnO, and NiO) with P25 and grounding in the ball mill (Mixer/Mill 8000 M, Spex, New York, NY, USA) to determine precisely the amount of dopants ions in the TiO_2 structure. Further crystal structure analysis was employed by Raman spectroscopy using the inVia Raman microscope (Renishaw plc, Wotton-under-Edge, UK). Plots of relative pressure vs. volume of adsorbed N_2 were obtained by a Nova 1200e sorptometer (Quantachrome Instruments, Boynton Beach, FL, USA). Transmission and scanning electron microscopy (TEM, SEM) techniques were used to characterize the morphology of doped-TiO_2 samples at Hitachi HT7700 microscope (Hitachi, Tokyo, Japan) and FEI Quanta FEG 250 (FEI Company, Hillsboro, OR, USA) operating at an accelerating voltage of 100 kV and 30 kV, respectively. Thermogravimetric analysis (TGA) was developed in the air atmosphere (30–1000 °C with a temperature ramp 10 °C/min) using Jupiter STA 449 F3 (Netzsch GmbH, Selb, Germany). Functional groups on the surface of investigated materials were determined using Fourier-transform infrared spectroscopy (FTIR) on an IFS-66/s spectrometer (Bruker, Billerica, MA, USA). Bandgaps were calculated based on diffuse-reflectance spectroscopy's (DRS) results obtained on Cary 5000 spectrometer (Varian, Palo Alto, CA, USA) equipped with an integrating sphere of diameter 100 mm. The surface chemical state and surface bonding were investigated *via* X-ray photoelectron spectroscopy (XPS) at an ultra-high vacuum on the SPECS Surface Nano Analysis GmbH spectrometer (Berlin, Germany). The paramagnetic centers were observed on electron paramagnetic resonance (EPR) spectra recorded at 77 K on an X-band (~8.9 GHz) CW-EPR SE/X-2547 spectrometer (Radiopan, Poznań, Poland) with 100 kHz modulation of a magnetic field and a reflection resonator. The photoelectrochemical parameters of prepared DSSCs, such as the current density and photovoltage characteristics (J-V), and electrochemical impedance spectroscopy (EIS), were recorded on Gamry Interface 1000 Potentiostat/Galvanostat/ZRA (Gamry Instruments, Warminster, PA, USA). The Sun 2000 class A Solar Simulator (ABET Technologies, Inc., Milford, MA, USA) was used as a light source under AM 1.5G (100 mW/cm^2) conditions. UV–vis spectroscopy was employed to determine the amount of dye adsorbed on working electrodes, carried on a Cary 50 spectrometer (Varian, Palo Alto, CA, USA). Incident photon to current conversion efficiency (IPCE) was investigated on Bentham PVE300 EQE/IPCE (Bentham Instruments Limited, Reading Berkshire, UK).

3. Results and discussion

3.1. Theoretical calculations

The structures of a pure and defected supercell of TiO_2 were relaxed using DFT/PBE + U methods. Hubbard correction parameters for Ti atoms equal to $U_{Ti} = 6$ eV and $J_{Ti} = 1$ eV were used the same as in our previous work [32]. Analyzing the crystal structure of pure α-TiO_2 using mentioned parameters was proved that the length of its unit cell increases by about 2% concerning the reference experimental structural data. Electronic properties of defected α-TiO_2 structures will be calculated by applying the $2 \times 2 \times 1$ TiO_2 supercell model. It was proved that the structural parameters of the supercell are consistent with experimental reference data. The ratio c/a of the cell length is the same as measured in the experiment. It is worth noticing that the total energy per atom for the $1 \times 1 \times 1$ TiO_2 and $2 \times 2 \times 1$ TiO_2 unit cells are practically the same. It means that the $2 \times 2 \times 1$ relaxed structure can be applied to study the electronic properties of defective systems based on α-TiO_2 (see Table 2).

Table 2

Structural parameters of the stoichiometric and nonstoichiometric α-TiO₂ calculated by the DFT/GGA + U methodology (U_{Ti} = 6.00 eV, U_{Mn} = 8.00 eV, U_{Cu} = 7.00 eV, U_{Ni} = 6.00 eV, and J_{Ti} = J_{Mn} = J_{Cu} = J_{Ni} = 1.00 eV) compared with reference experimental data.

Structure	a (a = b) [Å]	c [Å]	c/a	Total energy/atom [eV]
$1 \times 1 \times 1$ TiO₂	3.85	9.71	2.52	−8.74
Experimental reference data	3.79 [47,48]	9.51	2.51	−
	3.785 12(8) [49]	9.511 85(13)	2.513	
$2 \times 2 \times 1$ TiO₂	7.69 (3.85)	9.70	2.52	−8.73
$2 \times 2 \times 1$ TiO₂_v(Ti)	7.72 (3.86)	9.62	2.49	−8.43
$2 \times 2 \times 1$ TiO₂_v(O)	7.68 (3.84)	9.72	2.53	−8.70
$2 \times 2 \times 1$ TiO₂:Ni	7.68 (3.84)	9.64	2.51	−8.48
$2 \times 2 \times 1$ TiO₂:Ni_v(O)	a = 7.73 (3.86) b = 7.66 (3.83)	9.68	2.49 2.52	−8.52
$2 \times 2 \times 1$ TiO₂:Cu	7.71 (3.85)	9.66	2.51	−8.40
$2 \times 2 \times 1$ TiO₂:Cu_v(O)	a = 7.68 (3.84) b = 7.73 (3.86)	9.76	2.54 2.53	−8.46
$2 \times 2 \times 1$ TiO₂:Cu$_{in}$	7.75 (3.88)	9.67	2.49	−8.54
$2 \times 2 \times 1$ TiO₂:Mn	7.68 (3.84)	9.70	2.53	−8.50
$2 \times 2 \times 1$ TiO₂:Mn_v(O)	a = 7.69 (3.84) b = 7.73 (3.86)	9.78	2.54 2.53	−8.54
$2 \times 2 \times 1$ TiO₂:Mn$_{in}$	a = 7.72 (3.86) b = 7.74 (3.87)	9.73	2.52 2.51	−8.60

The main idea of the theoretical part of the present work was to model the structural and electronic properties of the TiO₂ crystals defected by dopants. Defects such as Cu, Mn, or Ni atoms were introduced into the crystal structure in a substitutive position of the Ti atom. The oxygen vacancies v(O) were investigated in metal ion-doped structures. Data presented in Table 2 shows that the titanium vacancies v(Ti) destabilize the TiO₂ structure creating the system with higher total energy per atom than calculated for the stoichiometric crystal. Analyzing the data presented in Table 2, one may see that the v(O) does not affect the crystal structure as it is done by v(Ti). It allows concluding that the α-TiO₂ crystal structure with the v(O) presence is very probable. In the case of the typical defects appearing in semiconducting crystals described as AB₂ structures, the v(O) does not make any significant crystallographic parameter changes compared with the pure structure. In addition, the energy per atom shows almost the same value as it was obtained for the non-defected structure. In contrast, in the case of v(Ti), critical changes in the structure are observed as significant decreases of the c/a and low crystal stability.

In Fig. S1 (Supplementary Information), the electron density differences for the crystals $2 \times 2 \times 1$ TiO₂_v(O) – $2 \times 2 \times 1$ TiO₂ are presented. One can see that the electron deficiency is seen in the place of the oxygen vacancy. The isosurface of electron density difference is also seen in the neighboring oxygen atoms. When the v(O) is created, the neighboring oxygens possess more electrons than is noticed for the stoichiometric crystal. The Ti atoms lying in the a-b plane close to v(O) are moving in the direction of vacancy, but the Ti atoms lying in the c direction close to vacancy are moving towards the vacancy. From these Ti atoms, electrons flow to oxygen atoms during vacancy formation. The movement of the Ti atoms located the closest to the v(O) influences the lattice structure modification of the $2 \times 2 \times 1$ TiO₂_v(O) structure contracting the structure in a and b direction and expanding it in the c direction.

Incorporating the Ni, Cu, and Mn dopants into the TiO₂ lattice increases the total structural energy per atom. However, the Mn-doped structure retains the most significant structural rigidity, and Cu doped

one stays with the lowest stability. It is worth noticing that the atom radius of Ti, Ni, Mn, and Cu atoms are 147, 125, 137, and 128 pm, respectively [50,51]. Therefore, it means that all dopants are smaller than Ti atoms. Consequently, the chosen dopants in the amount of 6% do not stabilize the $2 \times 2 \times 1$ supercell crystal model of the TiO₂. The Ni atoms as dopants are too small to correctly substitute the oxygen octahedral environment, and it shows significant changes in crystallographic parameters. In the case of Cu dopants, their bigger atom radius protects the structure from substantial changes. In contrast to the Ni and Cu dopants, the Mn atom saves the TiO₂ structure. It can be seen that the Mn atom can be added into a pure TiO₂ structure without any significant stress. The Ni dopants can be added to the TiO₂ structure only in a low concentration because they make considerable crystal stress. On the other hand, a higher concentration of Ni shows significant crystal instability.

The addition of the v(O) into doped crystals stabilizes their structures in all cases. It means that the structures with chosen metal dopants are more probable when the doping atoms are accompanied by v(O). In the case of Cu and Mn dopants, they were also introduced into the TiO₂ structure in the interstitial position, Cu$_{in,}$ and Mn$_{in}$, respectively. The Ni doped structure with atom added in interstitial position was not stable, and these structural parameters are not presented in Table 2. The Cu$_{in}$ and Mn$_{in}$ dopants stabilize the structures more than those introduced in substitutional positions, but the crystal structure parameters are more affected. Therefore, it was decided not to consider these structures by modeling them in coexistence with vacancies.

The α-TiO₂ crystal structure's electronic properties were correctly predicted using Hubbard parameters equal to U_{Ti} = 9.25 eV and J_{Ti} = 1.00 eV [32]. The energy gap calculated for the $(2 \times 2 \times 1)$ α-TiO₂ using mentioned parameters equals 3.18 eV when the corresponding experimental reference data is 3.20 eV. Consequently, the Hubbard parameters for dopants to calculate the electronic structures of modeled crystals were chosen as U_{Ni} = 6.00 eV, U_{Mn} = U_{Cu} = 7.00 eV, and for all atoms, the J = 1 eV. The electronic band structures of the α-TiO₂ crystal with Cu, Ni, and Mn dopants in substitutional positions are presented in Fig. 1. In all cases, added metal atoms create a double energy state in the bandgap, near 1 eV higher than the VB's maximum. Mostly d electrons of M^{2+} ions mixed with O 2p electrons create these additional energy states. In the case of Cu and Mn ions, one of the added energy levels is built by combining M^{2+} and Ti electrons because the dopants change their environment, acting on the first oxygen neighbors and second line of Ti neighbors. As the smallest dopant, the Ni does not act at the second line of neighbors built by Ti atoms. The electron density of states (DOS) (see Fig. S2 in the Supplementary Information) computed for these mentioned energy levels is relatively small compared to the remaining energy level. The DOS of discussed additional energy states calculated for the Cu dopants is constructed by spin-down electrons, while for Mn by spin-up electrons. Dopants almost do not change the energy state in the CB, but the VB is significantly affected by the Cu atoms. Changes in the VB affected by the p electrons system of the O atoms are not seen in the case of Ni and Mn dopants. The VB edge flattening by Cu atoms caused the higher effective mass of the holes compared to the pure or Mn and Ni-doped structures. The Ni and Cu dopants decrease the energy gap compared to the pure TiO₂ system, whereas the Mn ions do not change the value of the energy gap of the α-TiO₂. The Mn and Cu dopants lead to the preservation of the energy gap indirect-type, while the Ni atoms change it up to a direct one.

The pure α-TiO₂ and defected structure with v(O) exhibit an indirect bandgap, critical for photovoltaic properties. The v(O) gives an additional acceptor energy level created mainly by d electrons of Ti atoms mixed with p electrons of O atoms, with very low DOS [32]. The v(O) with Cu dopants make a critical change in the O p electron system, creating a VB (see Fig. 2). Because the v(O) increases the energy gap of the α-TiO₂ crystal structure (E_g = 3.28 eV) also, the bandgap of the Cu doped structure with v(O) is higher than the one of the Cu doped structure and is going to be direct with E_g = 3.20 eV. Here, the additional
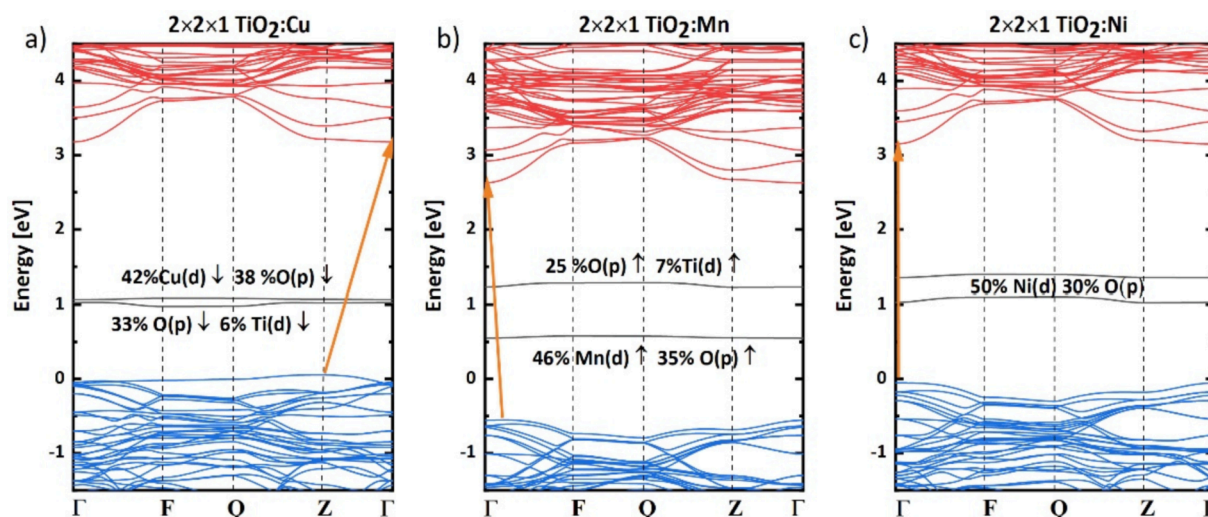
Fig. 1. Energy band structure calculated by DFT/PBE + U method for doped α-TiO$_2$, where Ti atoms were substituted by (a) Cu atoms (U$_{Ti}$ = 9.25 eV U$_{Cu}$ = 7.00 eV J$_{Ti}$ = J$_{Cu}$ = 1.00 eV), (b) Mn atoms (U$_{Ti}$ = 9.25 eV U$_{Mn}$ = 7.00 eV J$_{Ti}$ = J$_{Mn}$ = 1.00 eV), (c) Ni atoms (U$_{Ti}$ = 9.25 eV U$_{Ni}$ = 6.00 eV J$_{Ti}$ = J$_{Ni}$ = 1.00 eV).
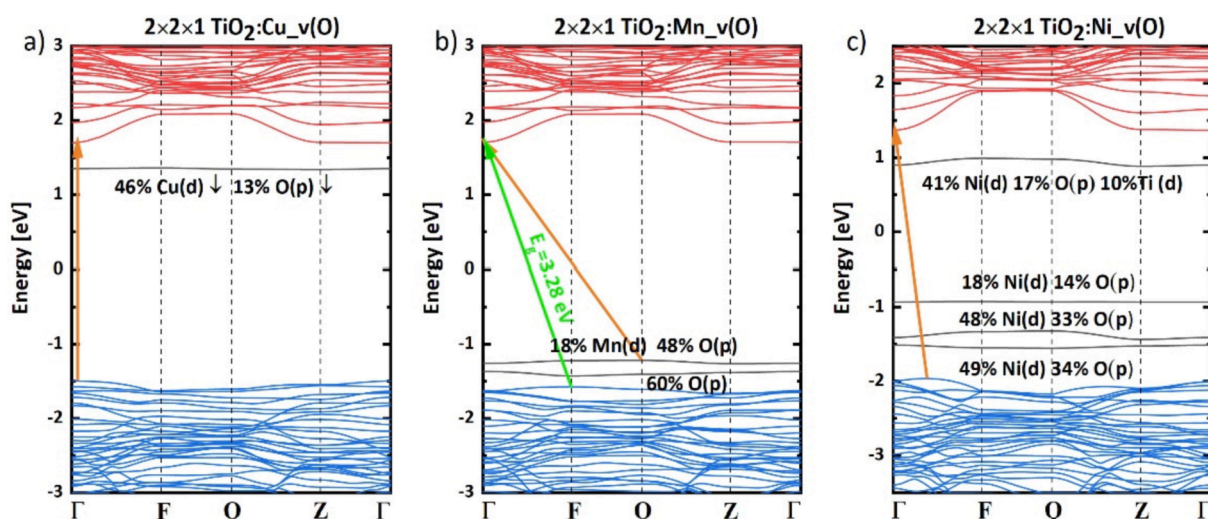
Fig. 2. Energy band structure calculated by DFT/PBE + U method for α-TiO$_2$ doped by transition metal atoms substituting Ti with presence of v(O) **(a)** Cu atoms (U$_{Ti}$ = 9.25 eV U$_{Cu}$ = 7.00 eV J$_{Ti}$ = J$_{Cu}$ = 1.00 eV), **(b)** Mn atoms (U$_{Ti}$ = 9.25 eV U$_{Mn}$ = 7.00 eV J$_{Ti}$ = J$_{Mn}$ = 1.00 eV), **(c)** Ni atoms (U$_{Ti}$ = 9.25 eV U$_{Ni}$ = 6.00 eV J$_{Ti}$ = J$_{Ni}$ = 1.00 eV).

donor energy level composed of *d* electrons of Cu was created. The mentioned energy state is almost flat, showing strong electron localization, and its dispersion does not depend on crystallographic direction. As seen for the Cu doped TiO$_2$, the donor energy level is constructed by spin-down electrons (see Fig. S3 in the Supplementary Information). In the donor state, as discussed above, the electron transfer is associated with a shortening charge carrier's lifetimes caused by strong recombination centers that destroy the material's photovoltaic properties.

Although, the Mn dopants with v(O) (see Fig. 2) show significant changes in *p* electrons of the O atoms. These changes give an additional doublet mixed *O(p)-Mn(d)* electron states, lowering the bandgap up to 2.92 eV, but the electron transition is becoming more indirect than the one of pure α-TiO$_2$ material. The acceptor energy levels are created by spin-down electrons (see Fig. S3 in the Supplementary Information).

The Ni dopants with v(O) do not show any significant changes in the O electron system compared with α-TiO$_2$ (see Fig. 2). A fundamental electron transition left indirect. The Ni dopants associated with v(O) add the donor and acceptor energy bands created mainly by the *d* electrons of Ni atoms. The acceptor band has higher DOS intensity (see Fig. S3 in

the Supplementary Information) than the donor states. The fundamental energy gap of this system (E_g = 3.33 eV) is higher than it is observed for TiO$_2$.

Analyzing the data presented in Fig. 3, one may conclude that the metal atoms decrease the CB edge except for the Ni dopants. All studied dopants associated with v(O) additionally reduce the edge of CB, which is convenient for photovoltaic applications. The most impressive change is seen for the TiO$_2$:Ni_v(O) material (in comparison to the structure without v(O)), which should go well with chosen dye.

The α-TiO$_2$ is an n-type semiconductor, and it can be seen by analyzing the conductivity (s/τ) versus chemical potential (see Fig. S4 in the Supplementary Information). The peaks at negative chemical potentials refer to n-type behavior, whereas positive chemical potentials refer to p-type behavior of the material. The electron conductivity (s/τ) calculated for the TiO$_2$ crystal (see Fig. S4a in the Supplementary Information) indicates the highest value at −4.66 eV, equal to 1.2×10^{20} $\Omega^{-1}cm^{-1}s^{-1}$. For the hole, the conductivity is the highest for 1.2 eV, with a value of 1.0×10^{20} $\Omega^{-1}cm^{-1}s^{-1}$. It is worth noticing that the conductivity for electrons and holes decreases for the TiO$_2$ with v(O) (Fig. S4b in the
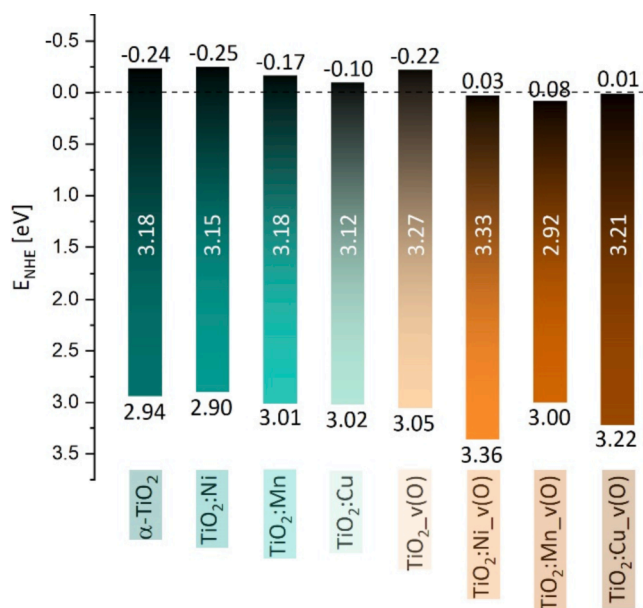
Fig. 3. CBs minima and VBs maxima for structures based on α-TiO$_2$ (modified with dopants and oxygen vacancies) and calculated by DFT/PBE + U method.

Supplementary Information). In pure α-TiO$_2$, the number of electrons is twice higher than the number of holes (see Fig. S5 in the Supplementary Information). Incorporating oxygen vacancies causes the number of electrons to decrease, keeping the same quantity of holes. In contrast to α-TiO$_2$, introducing Cu dopant into TiO$_2$ lattice leads to lower conductivity for holes and electrons. Moreover, the presence of the v(O) in the Cu-doped TiO$_2$ decreases the material's conductivity of holes and electrons twice (see Fig. S4c-d in the Supplementary Information). The conductivity of the Mn-doped structure and associated with v(O) is similar as it is observed for TiO$_2$ with Cu dopants (Fig. S4f in the Supplementary Information). Unexpectedly, for Ni-doped TiO$_2$, the share of hole conductivity increases. On the other hand, introducing the v(O) to this structure caused a decrease in hole conductivity while high energy electron conductivity rose (Fig. S4g-h in the Supplementary Information).

In the Cu-doped TiO$_2$ nanomaterial, the number of electrons slightly decreases with increasing the number of holes. The number of holes will be similar to the number of electrons. The v(O) presence in the Cu atom doped TiO$_2$ structure does not change the number of charge carriers (Fig. S5 in the Supplementary Information). Similar behavior is seen for the Mn dopant also associated with v(O). The Ni-doped TiO$_2$ possesses the number of charge carriers comparable with pure TiO$_2$. The v(O) decreases the number of electrons saving the number of hole carriers.

3.2. Experimental results

3.2.1. Physicochemical characterization

Optimization of sol–gel synthesis led to obtaining materials with similar transition metal ion content (about 0.4% based on XRF results), as shown in Table 3. Nonetheless, other samples listed in Table 1 were also characterized for a broader view of the problems raised at work, and their parameters can be found in the Supplementary Information.

Nanopowders of TiO$_2$:M^{2+} and corresponding working electrodes were investigated using the XRD technique, as shown in Fig. 4a (and Fig. S6 in the Supplementary Information). All tested materials crystallized in the form of anatase, which was confirmed by a 1–084-1285 reference pattern from the International Centre for Diffraction Data (ICDD). Moreover, well-defined reflexes can be attributed to the high crystallinity of the samples. Low-intense reflexes, visible mainly in powder-type samples, are assigned to the brookite phase (1–076-1937, ICDD). Sharp and narrow reflexes, observed in the series annealed on TCO substrates (TiO$_2$:M_FTO), come from the FTO and can be indicated as F-doped tin oxide (2–1337, ICDD). There are no significant shifts of the peaks after introducing dopants. However, there is a nanoparticles' downsizing tendency: 12.92, 11.21, and 9.65 nm corresponding to Ni^{2+}, Cu^{2+}, and Mn^{2+} dopant (values calculated using Scherrer equation). This slight discrepancy may be due to differences in atomic radius and inconsiderable variance in the concentration of dopants (Table 3) [52–54]. It is worth noticing that crystal size decrease with an increasing amount of metal ions, for instance, 11.21–9.39 nm or 9.65–8.36 nm corresponding to the Cu- and Mn-doped series except for the materials doped with Ni^{2+} ions (what can be explained by the lowest differences in dopant concentrations, see Table 1 and in the Table S1 Supplementary Information). Dubey et al. elucidated it as a disturbance of the periodicity of the TiO$_2$ crystal lattice by the metal ions remaining on the surface or grain boundary, which have not been able to enter into the matrix in the octahedral position [55]. Sharma and co-workers also indicate that the nanoparticles' size reduction may result from the emerging lattice defects and stacking errors [56]. On the other hand, there is a significant difference in crystal size after annealing pastes on the FTO substrate, which can be correlated with the migration of SnO$_2$:F nanoparticles into the TiO$_2$ layer and inhibition of further crystallites growth [32]. It is worth mentioning that there are no significant disorders in the crystal cell parameters (see Table 3 and in the Table S1 Supplementary Information), which stay in line with our theoretical calculation. However, as can be seen in Fig. S7 and (Table S2 Supplementary Information), there is a slight shift of the 101 plane to a higher angle after the incorporation of dopant ions into the TiO$_2$ lattice, which can be proof of the successful substitution of titanium atoms and as lattice contraction [57–59].

Raman spectra of M^{2+} ions doped TiO$_2$ are presented in Fig. 4b and Fig. S8 (Supplementary Information). It can be distinguished five intense peaks at about 145, 194, 397, 520, and 639 cm^{-1}, relating to anatase phase modes: E$_{g(1)}$, E$_{g(2)}$, B$_{1g(1)}$, A$_{1g}$/B$_{1g(2)}$, and E$_{g(3)}$, respectively [60]. Moreover, three additional peaks at around 246, 323, and 367 cm^{-1} are observed and attributed to the brookite residue (correlate with A$_{1g}$, B$_{1g}$, and B$_{2g}$, respectively) [61]. None of the other peaks is noticeable, as confirmed by the XRD results. It is worth noticing that in comparison to the undoped TiO$_2$ (143.5 cm^{-1}), a slight blue shift (1–3 cm^{-1}) of E$_{g(1)}$ vibrational mode after introducing metal ions was observed, as shown in (Table S3 Supplementary Information) [32]. Kernazhitsky et al. pointed out that this mode is susceptible to the O/Ti stoichiometric ratio and nanoparticle size [62]. Other phenomena such as phonon confinement, defects, and strain of crystal lattice also can affect the position and linewidth of Raman peaks [63]. As shown in Fig. 4b, the highest intensity of the E$_{g(1)}$ band among all the used dopant ions showed the TiO$_2$:Ni sample. Moreover, the further increase in the dopant content, seen in Fig. S8 (Supplementary Information), results in a decrease in the intensity of the E$_{g(1)}$ mode, with slight deviations in the TiO$_2$:Ni^{2+}/Cu^{2+}
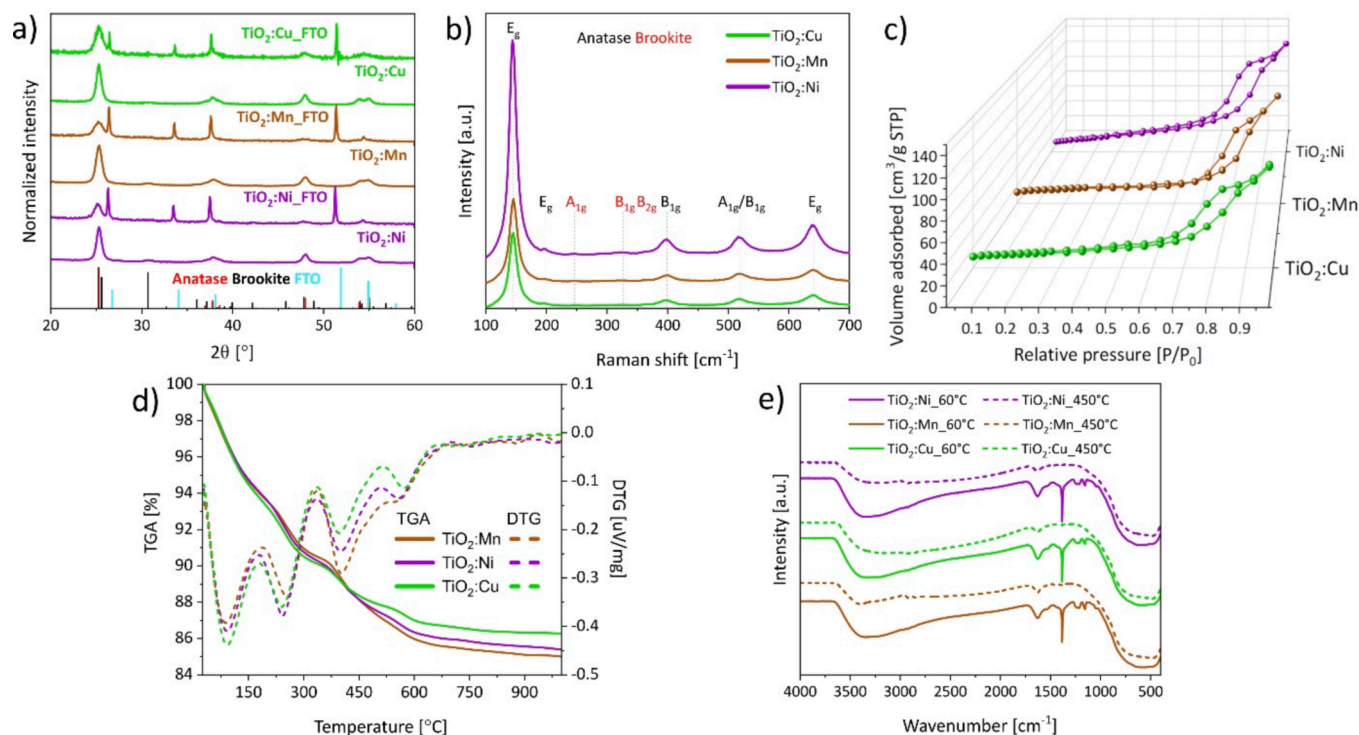
Table 3
Structural and photophysical parameters of as-prepared doped-TiO$_2$ samples.

Nanomaterial	M^{2+} [%]	D$_{hkl}$ [nm]	a = b [Å]	c [Å]	Cell vol. [Å^3]	A$_{BET}$ [m^2/g]	V$_p$ [cm^3/g]	S$_p$ [nm]	Ref.
TiO$_2$: Cu	0.421	11.21	3.79	9.51	136.53	45.6	0.204	8.1	This work
TiO$_2$: Mn	0.398	9.65	3.79	9.49	136.19	56.6	0.274	10.0	
TiO$_2$: Ni	0.377	12.92	3.79	9.51	136.45	63.7	0.219	9.3	
TiO$_2$	0	12.85	3.79	9.51	136.54	69.4	0.156	3.8	[32]

Fig. 4. (**a**) XRD patterns of TiO$_2$:M nanomaterials and corresponding photoanodes (TiO$_2$:M_FTO), (**b**) Raman spectra, (**c**) N$_2$ adsorption–desorption isotherms, (**d**) TGA (solid line) and DTG (dotted line) curves, (**e**) FTIR spectra of dried materials at 60 °C (solid line) and calcined at 450 °C (dotted line) of TiO$_2$:M.

series of prepared materials. Yang and Ma explain that incorporating metal ions inhibits the growth of TiO$_2$ nanoparticles, hence increasing internal stress and inhibiting lattice vibrations [63]. The full width at half maximum (FWHM) values also provide valuable information, because the smaller the bands' linewidth, the higher the crystallinity of the material. Based on our previous results, FWHM for undoped TiO$_2$ was 13.6 cm^{-1} [32]. After doping M^{2+} ions, the linewidth increased in order: TiO$_2$ undoped < TiO$_2$:Ni ≈ TiO$_2$:Cu < TiO$_2$:Mn. This phenomenon can also be seen with higher Cu^{2+} and Mn^{2+} ions content in the series (see in the Table S3Supplementary Information), except for Ni^{2+}-doped TiO$_2$ series. Based on theoretical calculations (see Table 2), the substituted Ni^{2+} ions cause significant discrepancies in the value of the c parameter among the tested ions, which may affect the crystallinity of the material [63]. Finally, phonon lifetime was also calculated using E$_g$ (1) mode, and a similar tendency to the FWHM values can be observed. The latter supports the occurrence of the phonon confinement effect, as discussed earlier, caused by decreasing nanoparticles sizes and imperfections in titania matrices [64].

The N$_2$ adsorption–desorption isotherms were recorded and shown in Fig. 4c and Fig. S9 (Supplementary Information) to investigate the textural properties of the tested materials. According to the IUPAC classification, isotherms' shapes are consistent with our previous results and may be assigned to the IVa isotherm type [32,65]. At higher relative pressure, characteristic triangle hysteresis loops with H2a shapes are observed in all investigated materials following IUPAC [65]. It proves that pores with various morphology formed interconnected networks leading to the formation of mesoporous type structure. It is seen in Table 3 that the surface area decreases in order Cu > Mn > Ni. That does not correspond unequivocally with the results obtained from XRD (nanoparticles' size). However, negligible differences in the percentage of metal ions content may affect the structural differences in these series. Summarizing the results obtained for all investigated TiO$_2$:M^{2+} series (based on in the Table S4Supplementary Information), the surface area varies between 45.6 and 79.6 m^2/g, while pore volumes and diameters are 0.159–0.376 cm^3/g, and 7.6–11.4 nm, respectively.

The annealing temperature of the samples for the production of

DSSCs was determined based on TGA as shown in Fig. 4d (and Fig. S10 in the Supplementary Information). Moreover, we distinguished four characteristic weight losses based on the derivative thermogravimetry (DTG) plots. At around 83–92 °C, the former can be assigned to the dehydration process. At about 240–258 °C, the second one is connected with the remaining from the M^{2+} sources nitrate ions' thermal decomposition to gases, e.g., NO, NO$_2$, N$_2$O, etc. [66]. Other weight losses observed in the graphs at 396–401 °C and 560–576 °C may be linked to decomposing organic substances and forming lattice defects, respectively. That is consistent with a choice of the 450 °C as the optimal calcination temperature applied during the DSSCs' manufacturing process.

The FTIR spectra, shown in Fig. 4e and Fig. S11 (Supplementary Information), confirmed the abovementioned considerations. After annealing, only three characteristic bands are visible: 450–660, 1631, and 3200–3400 cm^{-1}, where the first one is assigned to the metalloxane stretching vibrations M−O−M' (where M and M' are Ti, Cu, Mn, Ni), and the other two are linked to the hydroxyl groups [67,68]. In addition to these three bands, in a series of samples dried at a temperature of 60 °C, other peaks were observed, indicating possible reactions during the synthesis. Among others, bands at 1385, 2426, or 2852–2974 cm^{-1} are associated with σ(C-H) bonding (or nitrates ions), atmospheric CO$_2$, and –CH$_2$ symmetrical as well as –CH$_3$ asymmetrical stretching bonds, respectively [69,70]. The groups or compounds mentioned earlier come from the reagents present in the reaction medium, such as 2-propanol, metal nitrates, or CO$_2$ confined in the pores of titania nanopowders. Similar to our previous study, we also observe peaks connected with complexation reactions between metal ions and acetate groups. A signal at around 1155 cm^{-1} is associated with νM(O-C), while two inconsiderable bands at 1431 and 1527 cm^{-1} can be assigned to ν_{sym}COO and ν_{asym}COO vibrations, respectively [71,72]. Both peaks correspond to the formation of bidentate and bridging bondings between acetate and metal ions, proven by frequency separation around 100 cm^{-1} between them [72,73]. On the other hand, a wide band from 1211 to 1241 cm^{-1} (asymmetric stretching vibrations) may stem from creating ester – isopropyl acetate after M−O−M' species condensation reaction [73].

To better visualize the morphological properties of analyzed nanomaterials, TEM and SEM techniques were employed. As shown in Fig. 5, all obtained nanomaterials characterize the spherical shape of nanoparticles with a tendency to aggregate. Particles' size distributions calculated for all samples are narrow, and a growing trend: 11.30, 12.07, and 13.54 nm can be seen in series Mn > Cu > Ni, respectively, which also correlates with XRD results. However, differences can be seen between the data summarized in (Table S1Supplementary Information) and the size distribution's histograms shown in Fig. S12 (Supplementary Information). However, considering the standard deviation values, it can be assumed that the crystal sizes may be similar in all the samples. Returning to the morphology of the studied materials, as seen in SEM images (Fig. 5d-f), identical to TEM analysis, aggregates are observed in M^{2+} ions doped titania nanopowders. That process can be explained by minimizing the high surface energy of nanoparticles that stems from their nanosize [74]. It is worth noticing that characteristic pores are visible, confirming results obtained from the N_2 isotherm about forming a mesoporous-type structure.

The chemical composition and identification of oxidation states of the TiO_2:M materials were analyzed using the XPS method (Fig. 6). All spectra were corrected based on an adventitious carbon and set at 284.8 eV for the C-C/C-H band from the C 1s signal [75]. The photoelectron spectra of the C 1s signal (Fig. 6a) also show two other characteristic bands connected with C-O and O-C=O bondings occurring at 286.3 and 288.8 eV, respectively [76]. The latter being was not visible in the TiO_2: Ni nanomaterial. The observations mentioned above stay in line with our results obtained from FTIR measurements which indicate the presence of the organic residue on TiO_2:M nanoparticles.

In contrast, two prominent peaks are observed in the O 1s core-level spectrum (Fig. 6b) at about 530 eV and 531.6 eV. The former correlates with lattice oxygen, while the latter is assigned to the hydroxyl groups on the TiO_2 surface or defected TiO_2 [77]. The small band present at 533.2 eV in the TiO_2:Mn can be attributed to the oxygen in C-OH bonds [78]. As shown in Fig. 6c, a significant peak of Ti $2p_{3/2}$ at 458.6 eV with a splitting between Ti $2p_{1/2}$ and Ti $2p_{3/2}$ equal to 5.7 eV corresponds to anatase type structure [79]. Despite that, it is also worth noticing 2p spin–orbit doublets at 456.8 eV and 463 eV connected with Ti^{3+} ions (Fig. 6c, black arrows) [79]. During the heating, oxygen molecules break off titania nanoparticles' surface, and the resulting surplus of electrons reduces the titanium in the oxidation state 4+ to 3+ [80]. The oxygen

vacancy amount was calculated and presented in Table S5 (Supplementary Information) based on the peak areas [81]. The concentration of oxygen vacancies varies after incorporating dopant ions, which is a commonly known effect [23].

In Fig. 6d, three spectra of specific core-level regions: Cu 2p, Mn 2p, and Ni 2p, can be observed. The $2p_{3/2}$ peak in Fig. 6d (top) at 932.2 eV is typically assigned to the Cu^+ rather than Cu^{2+} ions [82]. Moreover, there are no visible satellites characteristic of Cu^{2+} ions. However, due to the low signal intensity and the noise visible in the spectrum, the oxidation state of the copper ion cannot be determined with certainty. Surprisingly, no Mn and Ni species are detected on the TiO_2 nanomaterials' surface. Sudrajat et al. explained that a high solubility of these ions into the bulk region forms a solid solution and decreases the ions' concentration on the TiO_2 surface [83]. It is also worth mentioning that it is not easy to measure Ni $2p_{3/2}$ binding energy on the TiO_2 surface, especially at such low metal ions content [84].

To better understand the nature of dopants in the TiO_2 matrices, EPR measurements were made at 77 K, as shown in Fig. 7 and Fig. S13 (Supplementary Information). The anisotropic spectrum shown in Fig. 7a presents two forms of Cu^{2+} ions: substituting Ti^{4+} ions in the matrices ($g_\perp$=2.078 and poorly separated quadruplet centered at g = 2.362) and present on the titania nanoparticles surface ($g_\perp$=2.099; g = 2.384) [85]. Moreover, the above-listed values of the g-factor are more significant than the g values of free electron (g_e = 2.0023). Their position indicates that Cu^{2+} ions are situated in an axially distorted octahedral coordination in TiO_2 lattice, consistent with our theoretical study (differences in the parameter c value in contrast to the 2 × 2 × 1 TiO_2 anatase) [86]. Moreover, charge compensation occurs with oxygen vacancies when substituting tetravalent ions with divalent metal [87]. However, the solid Cu^{2+} ion paramagnetic center signal can mask peaks connected with defects in titanium dioxide lattice. To sum up, EPR measurements unambiguously confirm the oxidation state of copper ions in TiO_2:Cu material to be 2+.

On the other hand, Fig. 7b exhibits TiO_2:Mn isotropic spectrum with central hyperfine sextet signals characteristic for disordered TiO_2 material doped with Mn^{2+} ions [88]. The shape and g = 2.000 factor distinguished in the spectrum also indicate matched substitution of Mn^{2+} ions in the TiO_2 lattice [89]. As shown in Table 2, the parameter c of the 2 × 2 × 1 TiO_2:Mn obtained from the theoretical calculations is similar to the undoped 2 × 2 × 1 TiO_2. Therefore, it does not disturb the

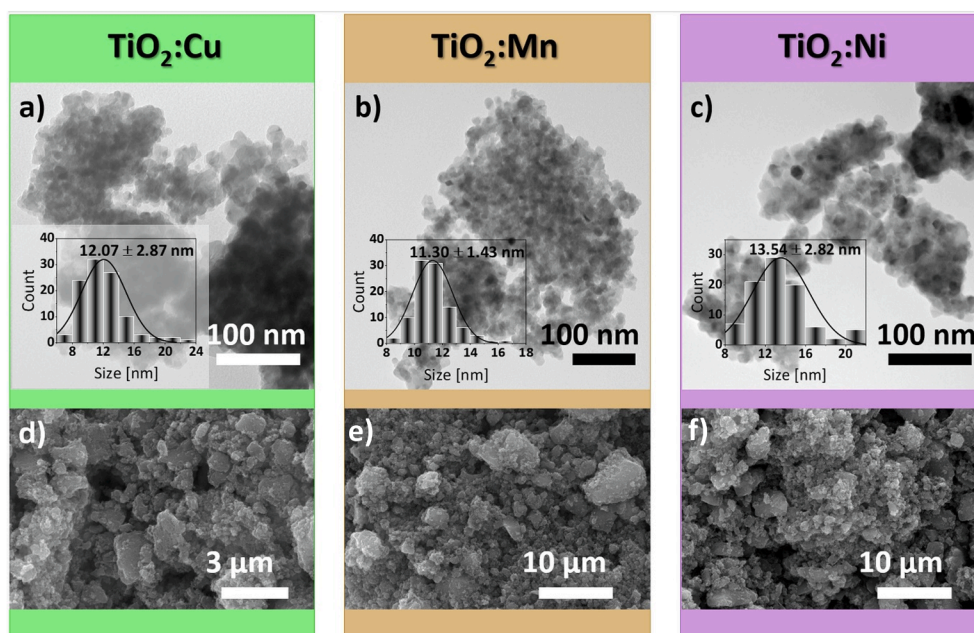**Fig. 5.** TEM **(a-c)** and SEM **(d-f)** images of TiO_2:M nanomaterials with inserted particles' size distribution histograms.
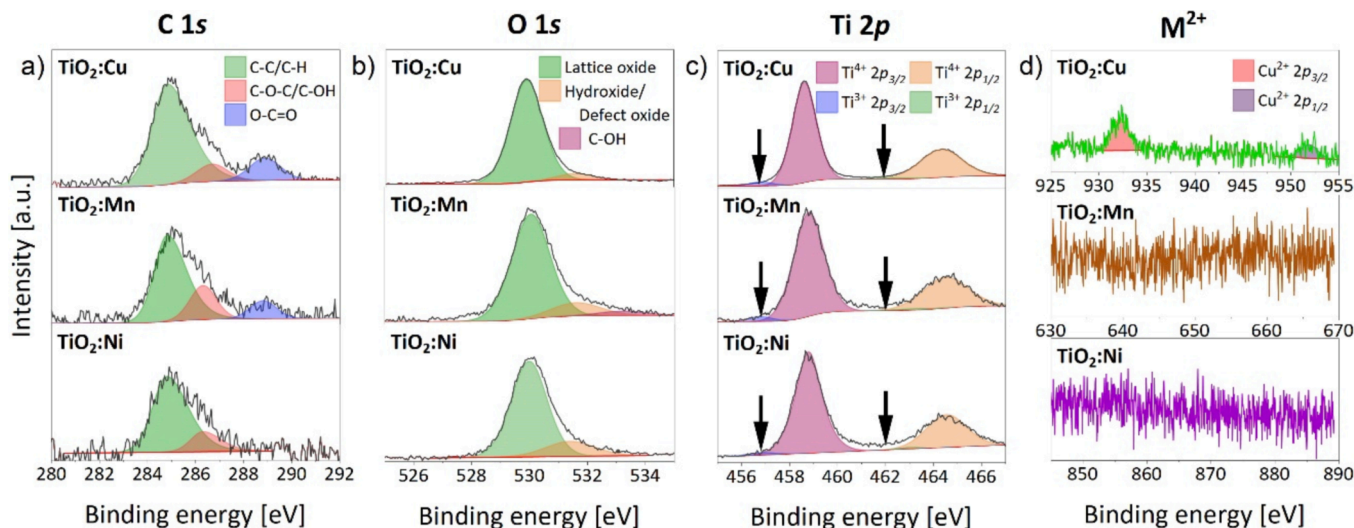
Fig. 6. XPS spectra of investigated nanomaterials with enlargement of following core-level regions: (**a**) C 1s, (**b**) O 1s, (**c**) Ti 2p, and (**d**) Cu (top), Mn (middle), Ni (bottom) 2p.
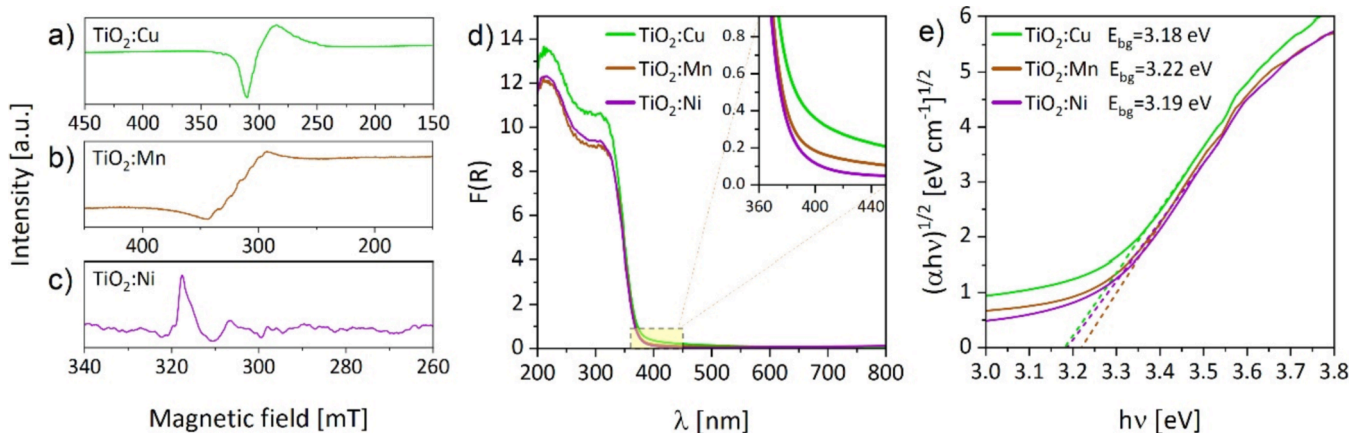

Fig. 7. EPR spectra of (**a**) TiO$_2$:Cu, (**b**) TiO$_2$:Mn, and (**c**) TiO$_2$:Ni nanomaterials; (**d**) Kubelka-Munk spectra with enlargement of specific range; (**e**) Tauc's plots of investigated TiO$_2$:M materials with extracted indirect energy bandgaps values.

titanium oxide structure, and the EPR measurements prove that. Identically to the TiO$_2$:Cu material, a poorly resolved spectrum of TiO$_2$:Mn is not allowed to observe other defects such as oxygen vacancies or the presence of Ti^{3+} ions in the material. Contrary to the above results in the TiO$_2$:Ni EPR spectrum (Fig. 7c), the characteristic peak g = 2.001 can be distinguished from the electrons trapped in oxygen vacancies and two peaks at g$_{\perp}$=2.062 and g = 2.133 coming from Ni$^+$ ions [90,91]. However, low intensity of Ni$^+$ peaks can result from a negligible amount of these species on the TiO$_2$ nanoparticles' surface connected with forming oxygen vacancies and metal ions reduction during heating processes.

Kubelka-Munk graphs presented in Fig. 7d and Fig. S14a (Supplementary Information) indicate intense absorption in the 200–400 nm range due to the charge transfer from the VB (combination of 2p oxide orbitals) to the CB (mainly formed by 3dt$_{2g}$ orbitals of Ti^{4+} ions) in TiO$_2$ structure [92]. After introducing dopant ions into TiO$_2$, a characteristic absorption edge redshift can be noticed. The optical bandgaps of tested materials were determined based on Tauc's plots presented in Fig. 7e and Fig. S14c-h (Supplementary Information). The bandgaps values were plotted using (αhν)$^{1/2}$ vs. (hν) and (αhν)^2 vs. (hν), which corresponds to the indirect- and direct type of bandgap, respectively. However, López and Gómez suggested that only the "indirect allowed transition" equation should be used for TiO$_2$ to avoid inconsistencies

[93]. As shown in Table S6 (Supplementary Information), data obtained from this equation for materials with around 0.4% content of M^{2+} are more related to our theoretical study (see Fig. 3). Even if the bandgaps values obtained in the experimental part of this work do not differ much from each other (3.18, 3.19, and 3.22 eV for Cu^{2+}, Ni^{2+}, and Mn^{2+} ions, respectively), we assume that energy bandgap structures with oxygen vacancies should be taken into consideration (Fig. 2). Moreover, it is worth mentioning that a higher concentration of particular ions leads to lowering bandgaps values (see Table S6 in the Supplementary Information), and it can explain theoretical end experimental discrepancies observed for the energy gap of the M^{2+} doped α-TiO$_2$ structure.

3.2.2. Photovoltaic characterization

Fig. 8a (and Fig. S15a-c in the Supplementary Information) shows J-V curves of DSSCs fabricated with TiO$_2$:M^{2+} nanomaterials, whose parameters are listed in Table 4 (and Table S7 in the Supplementary Information). It is commonly known that open-circuit photovoltage (V$_{OC}$) is mainly a potential difference between the semiconductor's Fermi level and the redox mediator's Nernst potential in the electrolyte (I$^-$/I$_3^-$ in this work) [94]. As the same electrolyte was used throughout the experiment, the CB edge (related to the Fermi level) and the electron density in the TiO$_2$ materials affect the V$_{OC}$ value changes. Introducing M^{2+} ions caused a drop of V$_{OC}$: 779.1, 777.1, 761.1, and 727.1 mV, corresponding
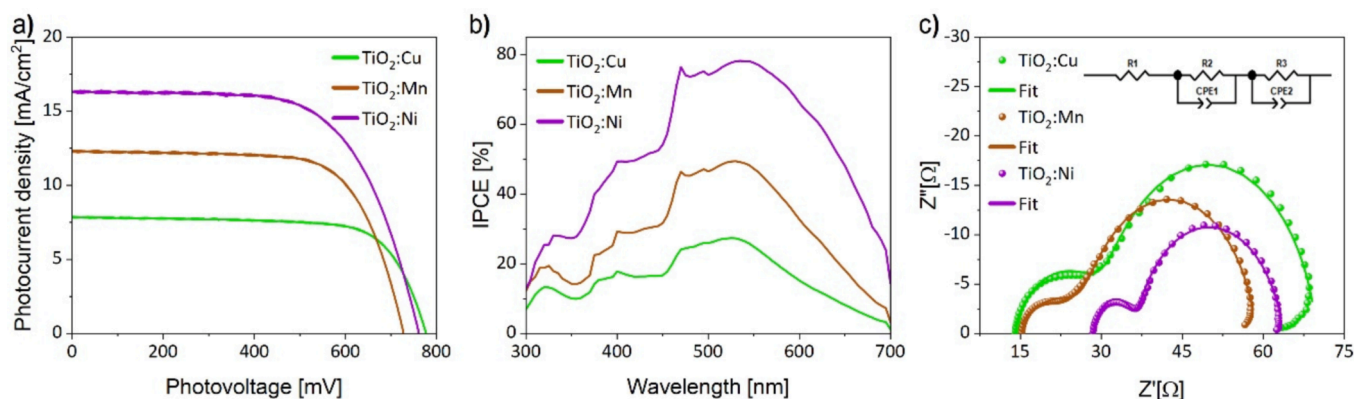
Fig. 8. (**a**) J-V characteristics, (**b**) IPCE spectra, and (**c**) Nyquist plots with inserted equivalent circuit model used for fitting.

Table 4
Photoelectrochemical parameters of investigated DSSCs.

Nanomaterial	V_{OC} [mV]	J_{SC} [mA/cm^2]	FF [%]	η [%]	N_{dye} [nmol/cm^2]	IPCE [%]	R_1 [Ω]	R_2 [Ω]	R_3 [Ω]	τ [ms]	Ref.
TiO$_2$:Cu	777.1	7.81	73.0	4.43	26.33	27.4	13.65	17.43	38.81	7.95	This work
TiO$_2$:Mn	727.1	12.24	70.3	6.25	19.77	49.4	14.24	14.06	30.37	12.76	
TiO$_2$:Ni	761.1	16.30	64.3	7.98	22.71	78.2	28.60	7.67	27.52	10.18	
TiO$_2$	779.1	13.50	70.4	7.41	16.62	68.6	17.34	4.79	30.79	10.18	[32]
P25	756.1	13.62	72.7	7.49	46.55	68.1	14.29	4.99	30.24	5.49	

to undoped TiO$_2$, TiO$_2$:Cu, TiO$_2$:Ni, and TiO$_2$:Mn, respectively. In other words, substituted ions led to positive shifting of the CB edge [95]. Our theoretical study can support that statement because, as shown in Fig. 3, introducing oxygen vacancy caused a significant positive shift of CB. However, it must be noted that VB maxima and CB minima calculated by the DFT/PBE + U method concern about 6% content of dopants (substitution of one titanium atom by M atom in the discussed TiO$_2$ supercell) and 6% of oxygen vacancies (removing of one oxygen atom) [32]. Therefore, the obtained experimental data do not unequivocally correspond to the theoretical calculations. For instance, our previous work showed that oxygen vacancies in undoped TiO$_2$ were formed mainly on the nanoparticles' surface during calcination, so a minor CB shift should be considered. Moreover, in every series of TiO$_2$:M^{2+} (Table S7 in the Supplementary Information), characteristic increases and then drop V_{OC} values are recorded. It may be induced by competition of oxygen vacancies and charge compensation influence.

Another investigated parameter, short-circuit photocurrent density (J_{SC}), depends on the light absorption and hence charge collection efficiency [96]. As shown in Table 4, TiO$_2$ doped with Ni^{2+} ions shows remarkable improvement of J_{SC} compared to other nanomaterials. It is also worth noticing the significant decrease of this factor in the case of TiO$_2$:Cu, which showed a slight difference in V_{OC} values towards the undoped or Ni-doped TiO$_2$. It suggests that V_{OC} is not directly proportional to J_{SC} in the cases studied. On the other hand, bearing in mind that J_{SC} is associated with the collection of sunlight, the relationship of this factor to the amount of adsorbed dye (N_{dye}) was first considered. Metal ions doping led to a reduction in the nanoparticles' sizes and surface area of the materials with a simultaneous three-fold increase in the pore diameter, referring to the structural data. Nevertheless, a more significant amount of dye molecules was noted on the doped nanomaterials' surfaces, which may be due to a change in the binding affinity of the dye to the doped-TiO$_2$ surface (see Fig. S16 in the Supplementary Information) [24,96,97].

Interestingly, although the obtained nanomaterials have N_{dye} values twice lower than P25, the example of TiO$_2$:Ni shows that it is not the decisive factor affecting the efficiency of the cells [98]. Therefore, it is worth paying attention to the fact that dopant ions incorporation increased sunlight-harvesting properties of synthesized doped-TiO$_2$ compared to P25. Moreover, Meng and Kaxiras, in their work, proposed

a thesis that oxygen vacancies present on TiO$_2$ surfaces may stabilize dye adsorption and influence charge injection processes [99]. Our previous work showed that introducing 3.7% Zr^{4+} ions into the TiO$_2$ crystal lattice lowered the CB edge to the optimal level, ensuring the most efficient electron injection process. The V_{OC} value for the constructed TiO$_2$:Ni cell is almost the same as when using TiO$_2$:3.7 %Zr (761.1 and 764.1 mV, respectively) [32]. It may indicate that we obtained a similar effect in this work by tailoring the electronic structure of the TiO$_2$-dye-electrolyte interface [32]. Based on the computational calculation, it might be assumed that additional donor–acceptor local centers (partly occupied) support electron transport. Moreover, oxygen vacancies present in the TiO$_2$:Ni structure caused a bandgap type change into indirect, which, together with donor–acceptor local centers mentioned above, increased charge carriers' mobility and J_{SC}.

It is worth noticing that further lowering of CB edge in the case of TiO$_2$:Mn (V_{OC} = 727.1 mV) concerning TiO$_2$:Ni (V_{OC} = 761.1 mV) does not show a positive influence on the J_{SC} factor. Although this positive shift stays in line with theoretical calculations (Fig. 3), conductivity properties should be taken under consideration to resolve discrepancies connected with the J_{SC}. As shown in Fig. S4 (Supplementary Information), the conductivity of electrons and holes in the TiO$_2$ doped with Mn and Cu ions after incorporating the v(O) decreases compared to the undoped system. At the same time, introducing Ni dopants with v(O) into the TiO$_2$ lattice caused a rise of conductivity, mainly electrons. That also explains the difference in the photocurrent density values between TiO$_2$:Ni and TiO$_2$:Cu nanomaterials, which energy bandgap structures nearby CB are pretty similar (Fig. 2).

Another crucial DSSC parameter, fill factor (FF), is regarded as a result of inherent resistance (especially shunt and series resistance – R_1) and defines the quality of hand-made solar cells [100,101]. Therefore, to better understand the data presented in Table 4, EIS measurements should be considered. Thus, dependencies between the total device resistance (R_t = R_1 + R_2 + R_3) and FF were plotted (Fig. S17a in the Supplementary Information). As can be seen, the lower R_t, the higher FF. However, there is an exception to the rule in the case of TiO$_2$:Cu fabricated DSSC. A more visible tendency can be seen in Fig. S17b (Supplementary Information), where only R_1 (series resistance) was considered. Therefore, the reduction in FF is mainly due to the discontinuities present on the conductive glass caused parasitic effect increasing resistance

[102]. Nevertheless, FF around 70% is a reasonable value reflecting the excellent quality typical for a hand-made DSSC [103].

The most measurable parameter in the DSSC characteristic is power conversion efficiency (η). As shown in Table S7 (Supplementary Information), the highest η values show nanomaterials with around 0.4% content of dopant ions and then drop with further increasing concentration. That may be related to the bandgap width, which decreases with increased M^{2+} ions content. However, a higher concentration of metal cations in all TiO_2:M^{2+} series leads to a V_{OC} increase and, hence, a negative CB shift (see Table S7 in the Supplementary Information). Due to the closer distance between the CB and the dye's LUMO level, electron injection has been decreased, affecting J_{SC} and hence η. On the other hand, the differences in the efficiency of the cells made of TiO_2:Mn, TiO_2:Ni, and TiO_2:Cu nanomaterials result from structural variations and the structure of the energy bandgap caused by the orbitals of individual metal ions [104].

The IPCE plots are revealed in Fig. 8b (and Fig. S15d-f in the Supplementary Information), and their data are also collected in Table 4 (and Table S7 in the Supplementary Information). In a few words, this technique allows the conversion efficiency of the incident photon converted to the solar cell's internal photocurrent to be determined at the proposed wavelength. As the working electrodes in this experiment are sensitized by N3 dye, their IPCE plots correspond to the absorption spectrum profile of the dye. The IPCE values read at a maximum of around 540 nm are related to the metal-to-ligand charge transfer band [105]. As shown in Table S7 (Supplementary Information), IPCE results parallel the J_{SC} values. Again, it can be concluded that mainly downward shift of the CB to the optimal level and specific energy bandgap structure enhance the electron injection and photocurrent, and decrease at the same time recombination of back-electron by the electrolyte [106].

The determination of charge transport kinetics and electron-hole recombination processes in tested cells have been made by EIS. Typically, EIS is expressed as a Bode or Nyquist plot, fitted simultaneously with the appropriate equivalent circuit model using specific software. Consequently, Nyquist plot analysis gives information about DSSC's internal resistance presented in the form of three semicircles (in this work, the last one called Warburg element connected with redox diffusion resistance, is not observed). The R_1 (from the Nyquist plot as the distance from zero to the first experimental point) is mainly caused by TCO substrate or wires connection. In contrast, one of the most critical resistances occurs in the TiO_2/dye/electrolyte interface (R_3, second semicircle), which directly affects the overall performance of the cells. As shown in Table 4, the higher R_3, the lower the overall DSSC efficiency is. The dramatic increase R_3 parameter in the case of TiO_2:Cu can be connected with the energy bandgap structure and redox reaction between Cu^{2+} ions on the nanoparticles' surface and iodide ions from the redox medium. Wherefore, recombination processes compete with charge transport, decreasing dye regeneration and hence η [107]. Moreover, that statement can be supported by the injected electron lifetime values (τ, estimated from the maximum frequency point of the second semicircle, based on the Bode diagram), which indicates extremely fast recombination with a higher concentration of Cu^{2+} ions in TiO_2 materials. As mentioned before, the conductivity of electrons and holes in the TiO_2:Cu nanomaterial is twice lower than in undoped TiO_2, which may also influence the R_3 value.

However, the trend connected with R_3 and η is not maintained in every series of doped nanomaterials (see Table S7 in the Supplementary Information). In the cases of TiO_2:Mn^{2+}/Ni^{2+} nanomaterials series, such a strong contribution of recombination processes does not appear. Here, it should be emphasized that the number of oxygen vacancies affects the charge recombination kinetics because a visible correlation between R_3 and V_{OC} can be observed. Subramanian et al. noticed that the back-electron recombination is suppressed with a higher R_3 value [106]. On the other hand, surface states and oxygen vacancies can act as recombination centers decreasing R_3 [106]. Therefore, it can be concluded that introducing M^{2+} ions at the beginning causes stress for TiO_2 matrice lattice and appearances of oxygen vacancies, then further increase the content of M^{2+} ions seek to charge compensation and the number of lattice defects decrease. Finally, after exceeding the appropriate amount of dopants in TiO_2 again, the number of oxygen vacancies increases. That statement aligns with V_{OC} values and theoretical considerations reflected in Fig. 3. The electron lifetimes for DSSCs made with 0.4% Mn^{2+} and Ni^{2+} ions content in the TiO_2 materials are also worth noticing. In the DSSC made with a TiO_2:Ni nanomaterial, the τ value is the same as pure TiO_2 and seems optimal. However, in the case of TiO_2:Mn, the longest τ was recorded. Probably, it may stem from the structural properties of this material, which indicate the smallest nanoparticles (9.65 nm), and at the same time, has the biggest pores diameters (10 nm) among other investigated nanomaterials. González–Verjan et al. noticed in their work that TiO_2 nanomaterial calcined at 250 °C showed 6.93 ± 0.59 nm nanoparticles with the highest in the mesoporous materials series pore diameter [108]. Moreover, they recorded the most extended electron lifetime of this material and elucidated this fact as confinement of electrons in the CB, thus lowering the efficiency of migration of these charge carriers through mesoscopic film, reducing the η of investigated DSSC [108]. Therefore, we suppose that a similar situation happened in the case of TiO_2:Mn.

Finally, it is worth paying attention to the tendency between R_3 and charge transfer resistance at the counter electrode/electrolyte interface (R_2, first semicircle) results because emerging recombination centers caused an increase of R_3 values and reduced charge transportation on the mentioned interface (a drop of R_2 values) [109,110]. Therefore, one may say that R_2 is a reflection of R_3 values. Moreover, R_2 and R_1 parameters are considered to have no major impact on the performance of the cells [45].

4. Conclusions

Based on computer calculations, it was found that the Cu^{2+}, Mn^{2+}, and Ni^{2+} ions substitute Ti^{4+} ions in the TiO_2 crystal lattice rather than inserted in the interstitial position. Moreover, we showed that highly favorable systems are those with oxygen vacancies due to charge compensation, based on lower total energy/atom values of particular forms. The experimental results confirmed the above conclusions. The TiO_2:M^{2+} nanomaterials were synthesized using modified sol–gel and optimized to obtain similar content of dopant ions to compare the properties of materials that differ only in the type of doped ion rather than their content. Anatase structure (with minor impurities of brookite) occurred in the tested samples, with nanoparticles' sizes below 15 nm. No rutile phase was observed, indicating that a 450°C annealing temperature was optimal. Based on electron microscopy research, spherical-shaped nanoparticles that tended to aggregate were recorded. Moreover, characteristic tunnels and pores were observed, proving the mesoporous structure of the materials (confirmed earlier by N_2 adsorption–desorption analysis). The method of incorporating dopants was established based on a combination of XPS and EPR techniques indicating substitution of M^{2+} ions into TiO_2 matrice, consistent with the theoretical assumptions.

Introducing M^{2+} ions also caused the bandgap narrowing (except for 0.4% of Mn^{2+} ions, which exhibit the same value as undoped TiO_2). Dopants and formed oxygen vacancies significantly rebuild the energy bandgap structure of investigated systems compared to undoped TiO_2. The above changes' influence was visible in the photovoltaic section, where obtained nanomaterials were used for DSSCs manufacturing. Again, a comprehensive analysis of the experimental data and computer calculations helped elucidate the electron transport mechanism in the studied structures. Moreover, we present a highly efficient DSSC made by TiO_2:Ni with a photoconversion efficiency improvement compared to standard P25.

CRediT authorship contribution statement

Aleksandra Bartkowiak: Conceptualization, Data curation, Formal analysis, Funding acquisition, Investigation, Methodology, Project administration, Resources, Validation, Visualization, Writing – original draft. **Oleksandr Korolevych:** Investigation, Methodology, Resources, Validation, Visualization, Writing – original draft. **Gian Luca Chiarello:** Resources, Supervision, Validation, Writing – original draft. **Malgorzata Makowska-Janusik:** Conceptualization, Funding acquisition, Investigation, Methodology, Project administration, Resources, Supervision, Validation, Writing – original draft. **Maciej Zalas:** Conceptualization, Funding acquisition, Investigation, Methodology, Project administration, Resources, Supervision, Validation, Writing – original draft.

Declaration of Competing Interest

The authors declare that they have no known competing financial interests or personal relationships that could have appeared to influence the work reported in this paper.

Acknowledgements

Appendix A. Supplementary material

Supplementary data to this article can be found online at https://doi.org/10.1016/j.apsusc.2022.153607.

References

[1] Y. Wu, C. Li, Z. Tian, J. Sun, Solar-driven integrated energy systems: State of the art and challenges, J. Power Sources. 478 (2020) 228762, https://doi.org/10.1016/j.jpowsour.2020.228762.

[2] F.-Q. Bai, W. Li, H.-X. Zhang, Theoretical Studies of Titanium Dioxide for Dye-Sensitized Solar Cell and Photocatalytic Reaction, in, Titan. Dioxide, InTech (2017) 229–248, https://doi.org/10.5772/intechopen.68745.

[3] M. Kokkonen, P. Talebi, J. Zhou, S. Asgari, S.A. Soomro, F. Elsehrawy, J. Halme, S. Ahmad, A. Hagfeldt, S.G. Hashmi, Advanced research trends in dye-sensitized solar cells, J. Mater. Chem. A. 9 (17) (2021) 10527–10545, https://doi.org/10.1039/D1TA00690H.

[4] B.D. Choudhury, C. Lin, S.M.A.Z. Shawon, J. Soliz-Martinez, H. Huq, M.J. Uddin, A photoanode with hierarchical nanoforest TiO₂ structure and silver plasmonic nanoparticles for flexible dye sensitized solar cell, Sci. Rep. 11 (2021) 7552, https://doi.org/10.1038/s41598-021-87123-z.

[5] B. O'Regan, M. Grätzel, A low-cost, high-efficiency solar cell based on dye-sensitized colloidal TiO₂ films, Nature. 353 (6346) (1991) 737–740, https://doi.org/10.1038/353737a0.

[6] G.S. Selopal, H.-P. Wu, J. Lu, Y.-C. Chang, M. Wang, A. Vomiero, I. Concina, E.-W.-G. Diau, Metal-free organic dyes for TiO₂ and ZnO dye-sensitized solar cells, Sci. Rep. 6 (2016) 18756, https://doi.org/10.1038/srep18756.

[7] M. Ramya, T.K. Nideep, V.P.N. Nampoori, M. Kailasnath, The impact of ZnO nanoparticle size on the performance of photoanodes in DSSC and QDSSC: a comparative study, J. Mater. Sci. Mater. Electron. 32 (3) (2021) 3167–3179, https://doi.org/10.1007/s10854-020-05065-0.

[8] A. Rajendran, S. Kandasamy, Synthesis and photovoltaic property characterization of CeO₂ film deposited on ITO substrate for dye sensitized solar cell, Mater. Res. Innov. 23 (2017) 1–7, https://doi.org/10.1080/14328917.2017.1349060.

[9] R. Gayathri, G. Raja, P. Rajeswaran, High stable with efficient dye-sensitized solar cell-based Al₂O₃/graphene hybrid photoanode fabricated by simple household microwave irradiation technique, J. Mater. Sci. Mater. Electron. 31 (12) (2020) 9742–9752, https://doi.org/10.1007/s10854-020-03520-6.

[10] P. Jayabal, V. Sasirekha, S. Mayandi, K. Jeganathan, V. Ramakrishnan, A facile hydrothermal synthesis of SrTiO₃ for dye sensitized solar cell application, J. Alloys Compd. 586 (2014) 456–461, https://doi.org/10.1016/j.jallcom.2013.10.012.

[11] M. Masjedi-Arani, M. Salavati-Niasari, Simple size-controlled fabrication of Zn₂SnO₄ nanostructures and study of their behavior in dye sensitized solar cells, Int. J. Hydrogen Energy. 42 (2) (2017) 858–866, https://doi.org/10.1016/j.ijhydene.2016.12.123.

[12] M.-E. Yeoh, K.-Y. Chan, Recent advances in photo-anode for dye-sensitized solar cells: a review, Int. J. Energy Res. 41 (15) (2017) 2446–2467, https://doi.org/10.1002/er.3764.

[13] P. Gnida, P. Jarka, P. Chulkin, A. Drygała, M. Libera, T. Tański, E. Schab-Balcerzak, Impact of TiO₂ Nanostructures on Dye-Sensitized Solar Cells Performance, Materials (Basel). 14 (2021) 1633, https://doi.org/10.3390/ma14071633.

[14] X. Hou, K. Aitola, P.D. Lund, TiO₂ nanotubes for dye-sensitized solar cells—A review, Energy Sci. Eng. (2020) 1–17, https://doi.org/10.1002/ese3.831.

[15] M. Zhang, T. Chen, Y. Wang, Insights into TiO₂ polymorphs: highly selective synthesis, phase transition, and their polymorph-dependent properties, RSC Adv. 7 (2017) 52755–52761, https://doi.org/10.1039/C7RA11515F.

[16] T. Zhu, S.-P. Gao, The Stability, Electronic Structure, and Optical Property of TiO₂ Polymorphs, J. Phys. Chem. C. 118 (21) (2014) 11385–11396, https://doi.org/10.1021/jp412462m.

[17] N.-G. Park, J. van de Lagemaat, A.J. Frank, Comparison of Dye-Sensitized Rutile- and Anatase-Based TiO₂ Solar Cells, J. Phys. Chem. B. 104 (38) (2000) 8989–8994, https://doi.org/10.1021/jp994365l.

[18] A. Mamakhel, J. Yu, F. Søndergaard-Pedersen, P. Hald, B.B. Iversen, Facile synthesis of brookite TiO₂ nanoparticles, Chem. Commun. 56 (95) (2020) 15084–15087, https://doi.org/10.1039/D0CC06795D.

[19] E. Lancelle-Beltran, P. Prené, C. Boscher, P. Belleville, P. Buvat, S. Lambert, F. Guillet, C. Marcel, C. Sanchez, Solid-State Organic/Inorganic Hybrid Solar Cells Based on Poly(octylthiophene) and Dye-Sensitized Nanobrookite and Nanoanatase TiO₂ Electrodes, Eur. J. Inorg. Chem. 2008 (6) (2008) 903–910, https://doi.org/10.1002/ejic.200701033.

[20] G.L. Chiarello, M.V. Dozzi, M. Scavini, J.-D. Grunwaldt, E. Selli, One step flame-made fluorinated Pt/TiO₂ photocatalysts for hydrogen production, Appl. Catal. B Environ. 160–161 (2014) 144–151, https://doi.org/10.1016/j.apcatb.2014.05.006.

[21] A. Zaleska, Doped-TiO₂: A Review, Recent Patents Eng. 2 (2008) 157–164, https://doi.org/10.2174/187221208786306289.

[22] H. Lin, C. Huang, W. Li, C. Ni, S. Shah, Y. Tseng, Size dependency of nanocrystalline TiO₂ on its optical property and photocatalytic reactivity exemplified by 2-chlorophenol, Appl. Catal. B Environ. 68 (1-2) (2006) 1–11, https://doi.org/10.1016/j.apcatb.2006.07.018.

[23] V. Kumaravel, S. Rhatigan, S. Mathew, M.C. Michel, J. Bartlett, M. Nolan, S. J. Hinder, A. Gascó, C. Ruiz-Palomar, D. Hermosilla, S.C. Pillai, Mo doped TiO₂: impact on oxygen vacancies, anatase phase stability and photocatalytic activity, J. Phys. Mater. 3 (2020), 025008, https://doi.org/10.1088/2515-7639/ab749c.

[24] T.S. Bramhankar, S.S. Pawar, J.S. Shaikh, V.C. Gunge, N.I. Beedri, P.K. Baviskar, H.M. Pathan, P.S. Patil, R.C. Kambale, R.S. Pawar, Effect of Nickel-Zinc Co-doped TiO₂ blocking layer on performance of DSSCs, J. Alloys Compd. 817 (2020), 152810, https://doi.org/10.1016/j.jallcom.2019.152810.

[25] G. Kresse, J. Furthmüller, Efficient iterative schemes for ab initio total-energy calculations using a plane-wave basis set, Phys. Rev. B. 54 (16) (1996) 11169–11186, https://doi.org/10.1103/PhysRevB.54.11169.

[26] G. Kresse, J. Furthmüller, Efficiency of ab-initio total energy calculations for metals and semiconductors using a plane-wave basis set, Comput. Mater. Sci. 6 (1) (1996) 15–50, https://doi.org/10.1016/0927-0256(96)00008-0.

[27] G. Kresse, D. Joubert, From ultrasoft pseudopotentials to the projector augmented-wave method, Phys. Rev. B. 59 (3) (1999) 1758–1775, https://doi.org/10.1103/PhysRevB.59.1758.

[28] J.P. Perdew, J.A. Chevary, S.H. Vosko, K.A. Jackson, M.R. Pederson, D.J. Singh, C. Fiolhais, Atoms, molecules, solids, and surfaces: Applications of the generalized gradient approximation for exchange and correlation, Phys. Rev. B. 46 (1992) 6671–6687, https://doi.org/10.1103/PhysRevB.46.6671.

[29] S. Hüfner, Electronic structure of NiO and related 3d-transition-metal compounds, Adv. Phys. 43 (2) (1994) 183–356, https://doi.org/10.1080/00018739400101495.

[30] A.I. Liechtenstein, V.I. Anisimov, J. Zaanen, Density-functional theory and strong interactions: Orbital ordering in Mott-Hubbard insulators, Phys. Rev. B. 52 (1995) R5467–R5470, https://doi.org/10.1103/PhysRevB.52.R5467.

[31] M.E. Arroyo-de Dompablo, A. Morales-García, M. Taravillo, DFT+ U calculations of crystal lattice, electronic structure, and phase stability under pressure of TiO₂ polymorphs, J. Chem. Phys. 135 (2011), 054503, https://doi.org/10.1063/1.3617244.

[32] A. Bartkowiak, O. Korolevych, G.L. Chiarello, M. Makowska-Janusik, M. Zalas, How Can the Introduction of Zr⁴⁺ Ions into TiO₂ Nanomaterial Impact the DSSC Photoconversion Efficiency? A Comprehensive Theoretical and Experimental Consideration, Materials (Basel). 14 (2021) 2955, https://doi.org/10.3390/ma14112955.

[33] W.-B. Zhang, Y.-H. Deng, Y.-L. Hu, K.-L. Han, B.-Y. Tang, Structural distortion of B1-structured MnO and FeO, Solid State Commun. 142 (2007) 6–9, https://doi.org/10.1016/j.ssc.2007.01.045.

[34] D. Wu, Q. Zhang, M. Tao, LSDA+U study of cupric oxide: Electronic structure and native point defects, Phys. Rev. B. 73 (2006), 235206, https://doi.org/10.1103/PhysRevB.73.235206.

[35] A. Rohrbach, J. Hafner, G. Kresse, Molecular adsorption on the surface of strongly correlated transition-metal oxides: A case study for CO/NiO(100), Phys. Rev. B. 69 (2004), 075413, https://doi.org/10.1103/PhysRevB.69.075413.

[36] H. Shin, Y. Luo, P. Ganesh, J. Balachandran, J.T. Krogel, P.R.C. Kent, A. Benali, O. Heinonen, Electronic properties of doped and defective NiO: A quantum Monte Carlo study, Phys. Rev. Mater. 1 (2017), 073603, https://doi.org/10.1103/PhysRevMaterials.1.073603.

[37] H.J. Monkhorst, J.D. Pack, Special points for Brillouin-zone integrations, Phys. Rev. B. 13 (12) (1976) 5188–5192, https://doi.org/10.1103/PhysRevB.13.5188.

[38] O. Jepson, O.K. Anderson, The electronic structure of h.c.p. Ytterbium, Solid State Commun. 88 (11-12) (1993) 871–875, https://doi.org/10.1016/0038-1098(93)90260-T.

[39] M. Methfessel, A.T. Paxton, High-precision sampling for Brillouin-zone integration in metals, Phys. Rev. B. 40 (6) (1989) 3616–3621, https://doi.org/10.1103/PhysRevB.40.3616.

[40] P.E. Blöchl, O. Jepsen, O.K. Andersen, Improved tetrahedron method for Brillouin-zone integrations, Phys. Rev. B. 49 (23) (1994) 16223–16233, https://doi.org/10.1103/PhysRevB.49.16223.

[41] C. Rödl, F. Fuchs, J. Furthmüller, F. Bechstedt, Quasiparticle band structures of the antiferromagnetic transition-metal oxides MnO, FeO, CoO, and NiO, Phys. Rev. B. 79 (2009), 235114, https://doi.org/10.1103/PhysRevB.79.235114.

[42] W.-B. Zhang, N. Yu, W.-Y. Yu, B.-Y. Tang, Stability and magnetism of vacancy in NiO: A GGA+U study, Eur. Phys. J. B. 64 (2) (2008) 153–158, https://doi.org/10.1140/epjb/e2008-00303-x.

[43] M. Nolan, S.D. Elliott, The p-type conduction mechanism in Cu₂O: a first principles study, Phys. Chem. Chem. Phys. 8 (45) (2006) 5350, https://doi.org/10.1039/b611969g.

[44] G.K.H. Madsen, D.J. Singh, BoltzTraP. A code for calculating band-structure dependent quantities, Comput. Phys. Commun. 175 (2006) 67–71. 10.1016/j.cpc.2006.03.007.

[45] A. Bartkowiak, B. Orwat, M. Zalas, P. Ledwon, I. Kownacki, W. Tejchman, 2-Thiohydantoin Moiety as a Novel Acceptor/Anchoring Group of Photosensitizers for Dye-Sensitized Solar Cells, Materials (Basel). 13 (2020) 2065, https://doi.org/10.3390/ma13092065.

[46] M. Zalas, K. Jelak, Optimization of platinum precursor concentration for new, fast and simple fabrication method of counter electrode for DSSC application, Optik (Stuttg). 206 (2020) 164314, https://doi.org/10.1016/j.ijleo.2020.164314.

[47] J.K. Burdett, T. Hughbanks, G.J. Miller, J.V. Smith, J.W. Richardson, Structural-Electronic Relationships in Inorganic Solids: Powder Neutron Diffraction Studies of the Rutile and Anatase Polymorphs of Titanium Dioxide at 15 and 295 K, J. Am. Chem. Soc. 109 (1987) 3639–3646, https://doi.org/10.1021/ja00246a021.

[48] K.V.K. Rao, S.V.N. Naidu, LEELA Iyengar, Thermal Expansion of Rutile and Anatase, J. Am. Ceram. Soc. 53 (3) (1970) 124–126.

[49] T. Arlt, M. Bermejo, M. Blanco, High-pressure polymorphs of anatase, Phys. Rev. B - Condens. Matter Mater. Phys. 61 (2000) 14414–14419, https://doi.org/10.1103/PhysRevB.61.14414.

[50] A.F. Wells, Structural inorganic chemistry, 5th edition, Oxford: Clarendon Press, 1984.

[51] R.D. Shannon, Revised effective ionic radii and systematic studies of interatomic distances in halides and chalcogenides, Acta Crystallogr. Sect. A. 32 (5) (1976) 751–767, https://doi.org/10.1107/S0567739476001551.

[52] R. Kayestha, K.H. Sumati, Esr,, studies on the effect of ionic radii on displacement of Mn²⁺ bound to a soluble β-galactoside binding hepatic lectin, FEBS Lett. 368 (1995) 285–288, https://doi.org/10.1016/0014-5793(95)00673-W.

[53] I. Ganesh, A.K. Gupta, P.P. Kumar, P.S.C. Sekhar, K. Radha, G. Padmanabham, G. Sundararajan, Preparation and characterization of Ni-doped TiO₂ materials for photocurrent and photocatalytic applications, Sci. World J. 2012 (2012), https://doi.org/10.1100/2012/127326.

[54] A. Pérez-Larios, A. Hernández-Gordillo, G. Morales-Mendoza, L. Lartundo-Rojas, Á. Mantilla, R. Gómez, Enhancing the H₂ evolution from water-methanol solution using Mn²⁺-Mn⁺³-Mn⁴⁺ redox species of Mn-doped TiO₂ sol-gel photocatalysts, Catal. Today. 266 (2016) 9–16, https://doi.org/10.1016/j.cattod.2015.12.029.

[55] R.S. Dubey, S. Singh, Investigation of structural and optical properties of pure and chromium doped TiO₂ nanoparticles prepared by solvothermal method, Results Phys. 7 (2017) 1283–1288, https://doi.org/10.1016/j.rinp.2017.03.014.

[56] A. Sharma, M. Varshney, H.-J. Shin, B.-H. Lee, K.H. Chae, S.O. Won, Effect of Cu insertion on structural, local electronic/atomic structure and photocatalyst properties of TiO₂, ZnO and Ni(OH)₂ nanostructures: XANES-EXAFS study, Mater. Chem. Phys. 191 (2017) 129–144, https://doi.org/10.1016/j.matchemphys.2017.01.008.

[57] S.A. Acharya, V.M. Gaikwad, V. Sathe, S.K. Kulkarni, Influence of gadolinium doping on the structure and defects of ceria under fuel cell operating temperature, Appl. Phys. Lett. 104 (2014), 113508, https://doi.org/10.1063/1.4869116.

[58] E. Akman, S. Akin, T. Ozturk, B. Gulveren, S. Sonmezoglu, Europium and terbium lanthanide ions co-doping in TiO₂ photoanode to synchronously improve light-harvesting and open-circuit voltage for high-efficiency dye-sensitized solar cells, Sol. Energy. 202 (2020) 227–237, https://doi.org/10.1016/j.solener.2020.03.108.

[59] J.H. Lim, S.M. Lee, H.-S. Kim, H.Y. Kim, J. Park, S.-B. Jung, G.C. Park, J. Kim, J. Joo, Synergistic effect of Indium and Gallium co-doping on growth behavior and physical properties of hydrothermally grown ZnO nanorods, Sci. Rep. 7 (2017) 41992, https://doi.org/10.1038/srep41992.

[60] K.-R. Zhu, M.-S. Zhang, Q. Chen, Z. Yin, Size and phonon-confinement effects on low-frequency Raman mode of anatase TiO₂ nanocrystal, Phys. Lett. A. 340 (1-4) (2005) 220–227, https://doi.org/10.1016/j.physleta.2005.04.008.

[61] G.A. Tompsett, G.A. Bowmaker, R.P. Cooney, J.B. Metson, K.A. Rodgers, J.M. Seakins, The Raman spectrum of brookite, TiO₂ (Pbca, Z = 8), J. Raman Spectrosc. 26 (1) (1995) 57–62, https://doi.org/10.1002/jrs.1250260110.

[62] L. Kernazhitsky, V. Shymanovska, T. Gavrilko, V. Naumov, L. Fedorenko, V. Kshnyakin, J. Baran, Room temperature photoluminescence of anatase and rutile TiO₂ powders, J. Lumin. 146 (2014) 199–204, https://doi.org/10.1016/j.jlumin.2013.09.068.

[63] C.-H. Yang, Z.-Q. Ma, Raman spectral analysis of TiO₂ thin films doped with rare-earth samarium, Appl. Opt. 51 (2012) 5438, https://doi.org/10.1364/AO.51.005438.

[64] B. Choudhury, A. Choudhury, Local structure modification and phase transformation of TiO₂ nanoparticles initiated by oxygen defects, grain size, and annealing temperature, Int. Nano Lett. 3 (2013) 55, https://doi.org/10.1186/2228-5326-3-55.

[65] M. Thommes, K. Kaneko, A.V. Neimark, J.P. Olivier, F. Rodriguez-Reinoso, J. Rouquerol, K.S.W. Sing, Physisorption of gases, with special reference to the evaluation of surface area and pore size distribution (IUPAC Technical Report), Pure Appl. Chem. 87 (2015) 1051–1069, https://doi.org/10.1515/pac-2014-1117.

[66] E.A. Cochran, K.N. Woods, D.W. Johnson, C.J. Page, S.W. Boettcher, Unique chemistries of metal-nitrate precursors to form metal-oxide thin films from solution: materials for electronic and energy applications, J. Mater. Chem. A. 7 (2019) 24124–24149, https://doi.org/10.1039/C9TA07727H.

[67] C.G. Silva, M.J. Sampaio, R.R.N. Marques, L.A. Ferreira, P.B. Tavares, A.M.T. Silva, J.L. Faria, Photocatalytic production of hydrogen from methanol and saccharides using carbon nanotube-TiO₂ catalysts, Appl. Catal. B Environ. 178 (2015) 82–90, https://doi.org/10.1016/j.apcatb.2014.10.032.

[68] Z. Liu, Z. Jian, J. Fang, X. Xu, X. Zhu, S. Wu, Low-Temperature Reverse Microemulsion Synthesis, Characterization, and Photocatalytic Performance of Nanocrystalline Titanium Dioxide, Int. J. Photoenergy. 2012 (2012) 1–8, https://doi.org/10.1155/2012/702503.

[69] A.C. Taş, P.J. Majewski, F. Aldinger, Synthesis of Gallium Oxide Hydroxide Crystals in Aqueous Solutions with or without Urea and Their Calcination Behavior, J. Am. Ceram. Soc. 85 (2002) 1421–1429, https://doi.org/10.1111/j.1151-2916.2002.tb00291.x.

[70] E. Pretsch, P. Buhlmann, M. Badertscher, Structure Determination of Organic Compounds, Springer, Berlin Heidelberg, Berlin, Heidelberg (2009), https://doi.org/10.1007/978-3-540-93810-1.

[71] M.T. Colomer, Straightforward synthesis of Ti-doped YSZ gels by chemical modification of the precursors alkoxides, J. Sol-Gel Sci. Technol. 67 (1) (2013) 135–144, https://doi.org/10.1007/s10971-013-3059-9.

[72] S. Doeuff, M. Henry, C. Sanchez, J. Livage, Hydrolysis of titanium alkoxides: Modification of the molecular precursor by acetic acid, J. Non. Cryst. Solids. 89 (1987) 206–216, https://doi.org/10.1016/S0022-3093(87)80333-2.

[73] K. Elghniji, Z. Anna-Rabah, E. Elaloui, Novel and facile synthesis of transparent-monolithic TiO₂ gels by sol-gel method based on an esterification reaction, Mater. Sci. 34 (2016) 633–640, https://doi.org/10.1515/msp-2016-0091.

[74] S. Shrestha, B. Wang, P. Dutta, Nanoparticle processing: Understanding and controlling aggregation, Adv. Colloid Interface Sci. 279 (2020) 102162, https://doi.org/10.1016/j.cis.2020.102162.

[75] J.F. Moulder, W.F. Stickle, P.E. Sobol, K.D. Bomben, Handbook of X-ray Photoelectron Spectroscopy: A Reference Book of Standard Spectra for Identification and Interpretation of XPS Data, Physical Electronics Division, Perkin-Elmer Corporation, United States of America, 1992.

[76] H. Liu, L. Liu, Z. Zhang, X. Dong, T. Liu, Hydrothermal etching fabrication of TiO₂@graphene hollow structures: mutually independent exposed 001 and 101 facets nanocrystals and its synergistic photocaltalytic effects, Sci. Rep. 6 (2016) 33839, https://doi.org/10.1038/srep33839.

[77] A. Wiatrowski, M. Obstarczyk, A. Obstarczyk, D. Wojcieszak, D. Kaczmarek, J. Morgiel, D. Gibson, Comparison of the Physicochemical Properties of TiO₂ Thin Films Obtained by Magnetron Sputtering with Continuous and Pulsed Gas Flow, Coatings. 8 (2018) 412, https://doi.org/10.3390/coatings8110412.

[78] Y. Chen, H. Wang, B. Dang, Y. Xiong, Q. Yao, C. Wang, Q. Sun, C. Jin, Bio-Inspired nacre-like nanolignocellulose-poly (vinyl alcohol)-TiO₂ composite with superior mechanical and photocatalytic properties, Sci. Rep. 7 (2017) 1823, https://doi.org/10.1038/s41598-017-02082-8.

[79] M.C. Biesinger, L.W.M. Lau, A.R. Gerson, R.S.C. Smart, Resolving surface chemical states in XPS analysis of first row transition metals, oxides and hydroxides: Sc, Ti, V, Cu and Zn, Appl. Surf. Sci. 257 (3) (2010) 887–898, https://doi.org/10.1016/j.apsusc.2010.07.086.

[80] S. Livraghi, M. Chiesa, M.C. Paganini, E. Giamello, On the Nature of Reduced States in Titanium Dioxide As Monitored by Electron Paramagnetic Resonance. I: The Anatase Case, J. Phys. Chem. C. 115 (51) (2011) 25413–25421, https://doi.org/10.1021/jp209075m.

[81] X. Bi, G. Du, A. Kalam, D. Sun, Y. Yu, Q. Su, B. Xu, A.G. Al-Sehemi, Tuning oxygen vacancy content in TiO₂ nanoparticles to enhance the photocatalytic performance, Chem. Eng. Sci. 234 (2021) 116440, https://doi.org/10.1016/j.ces.2021.116440.

[82] G. Pedroza-Herrera, I.E. Medina-Ramírez, J.A. Lozano-Álvarez, S.E. Rodil, Evaluation of the Photocatalytic Activity of Copper Doped TiO₂ nanoparticles for the Purification and/or Disinfection of Industrial Effluents, Catal. Today. 341 (2020) 37–48, https://doi.org/10.1016/j.cattod.2018.09.017.

[83] H. Sudrajat, S. Babel, A.T. Ta, T.K. Nguyen, Mn-doped TiO₂ photocatalysts: Role, chemical identity, and local structure of dopant, J. Phys. Chem. Solids. 144 (2020), 109517, https://doi.org/10.1016/j.jpcs.2020.109517.

[84] J.S. Pan, J.G. Tao, C.H.A. Huan, S.Y. Chiam, Z. Zhang, D.T.H. Li, Y. Sun, J.W. Chai, S.J. Wang, C.Q. Sun, Determination of atomic Ni interaction with TiO₂ by XPS, Surf. Interface Anal. 42 (2010) 878–881, https://doi.org/10.1002/sia.3356.

[85] K. Bhattacharyya, G.P. Mane, V. Rane, A.K. Tripathi, A.K. Tyagi, Selective CO_2 Photoreduction with Cu-Doped TiO_2 Photocatalyst: Delineating the Crucial Role of Cu-Oxidation State and Oxygen Vacancies, J. Phys. Chem. C. 125 (2021) 1793–1810, https://doi.org/10.1021/acs.jpcc.0c08441.

[86] B. Choudhury, M. Dey, A. Choudhury, Defect generation, d-d transition, and band gap reduction in Cu-doped TiO_2 nanoparticles, Int. Nano Lett. 3 (2013) 25, https://doi.org/10.1186/2228-5326-3-25.

[87] G. Li, N.M. Dimitrijevic, L.e. Chen, T. Rajh, K.A. Gray, Role of Surface/Interfacial Cu^{2+} Sites in the Photocatalytic Activity of Coupled $CuO-TiO_2$ Nanocomposites, J. Phys. Chem. C. 112 (48) (2008) 19040–19044, https://doi.org/10.1021/jp8068392.

[88] S.K. Misra, Interpretation of Mn^{2+} EPR spectra in disordered Materials, Appl. Magn. Reson. 10 (1-3) (1996) 193–216, https://doi.org/10.1007/BF03163109.

[89] N. Sakaguchi Miyamoto, R. Miyamoto, E. Giamello, T. Kurisaki, H. Wakita, Evaluation of coexistent metal ions with TiO_2: an EPR approach, Res. Chem. Intermed. 44 (7) (2018) 4563–4575, https://doi.org/10.1007/s11164-018-3468-z.

[90] E. Serwicka, ESR study on the interaction of water vapour with polycrystalline TiO_2 under illumination, Colloids and Surfaces. 13 (1985) 287–293, https://doi.org/10.1016/0166-6622(85)80028-7.

[91] S.-H. Chien, Y.-W. Wei, M.-C. Lin, EPR Studies of Photoreduction of Ni/TiO_2 Catalysts, J. Chinese Chem. Soc. 44 (3) (1997) 195–201, https://doi.org/10.1002/jccs.199700031.

[92] N. Venkatachalam, M. Palanichamy, V. Murugesan, Sol-gel preparation and characterization of nanosize TiO_2: Its photocatalytic performance, Mater. Chem. Phys. 104 (2-3) (2007) 454–459, https://doi.org/10.1016/j.matchemphys.2007.04.003.

[93] R. López, R. Gómez, Band-gap energy estimation from diffuse reflectance measurements on sol–gel and commercial TiO_2: a comparative study, J. Sol-Gel Sci. Technol. 61 (2012) 1–7, https://doi.org/10.1007/s10971-011-2582-9.

[94] J. Yao, C.-M. Lin, S. (Shizhuo) Yin, P. Ruffin, C. Brantley, E. Edwards, High open-circuit voltage dye-sensitized solar cells based on a nanocomposite photoelectrode, J. Photonics Energy. 5 (2015) 053088. 10.1117/1.JPE.5.053088.

[95] A.E. Shalan, M.M. Rashad, Incorporation of Mn^{2+} and Co^{2+} to TiO_2 nanoparticles and the performance of dye-sensitized solar cells, Appl. Surf. Sci. 283 (2013) 975–981, https://doi.org/10.1016/j.apsusc.2013.07.055.

[96] B. Roose, S. Pathak, U. Steiner, Doping of TiO_2 for sensitized solar cells, Chem. Soc. Rev. 44 (22) (2015) 8326–8349, https://doi.org/10.1039/C5CS00352K.

[97] C. Bauer, G. Boschloo, E. Mukhtar, A. Hagfeldt, Ultrafast studies of electron injection in Ru dye sensitized SnO_2 nanocrystalline thin film, Int. J. Photoenergy. 4 (2002) 17–20, https://doi.org/10.1155/S1110662X0200003X.

[98] J. Jiu, F. Wang, M. Sakamoto, J. Takao, M. Adachi, Performance of dye-sensitized solar cell based on nanocrystals TiO_2 film prepared with mixed template method, Sol. Energy Mater. Sol. Cells. 87 (1-4) (2005) 77–86, https://doi.org/10.1016/j.solmat.2004.06.011.

[99] S. Meng, E. Kaxiras, Electron and Hole Dynamics in Dye-Sensitized Solar Cells: Influencing Factors and Systematic Trends, Nano Lett. 10 (2010) 1238–1247, https://doi.org/10.1021/nl100442e.

[100] A. Kubiak, Z. Bielan, A. Bartkowiak, E. Gabała, A. Piasecki, M. Zalas, A. Zielińska-Jurek, M. Janczarek, K. Siwińska-Ciesielczyk, T. Jesionowski, Synthesis of Titanium Dioxide via Surfactant-Assisted Microwave Method for Photocatalytic and Dye-Sensitized Solar Cells Applications, Catalysts. 10 (2020) 586, https://doi.org/10.3390/catal10050586.

[101] L.B. Patle, V.R. Huse, A.L. Chaudhari, Band edge movement and structural modifications in transition metal doped TiO_2 nanocrystals for the application of DSSC, Mater. Res. Express. 4 (2017) 105045, https://doi.org/10.1088/2053-1591/aa919a.

[102] D. Pysch, A. Mette, S.W. Glunz, A review and comparison of different methods to determine the series resistance of solar cells, Sol. Energy Mater. Sol. Cells. 91 (18) (2007) 1698–1706, https://doi.org/10.1016/j.solmat.2007.05.026.

[103] P.K. Nayak, G. Garcia-Belmonte, A. Kahn, J. Bisquert, D. Cahen, Photovoltaic efficiency limits and material disorder, Energy Environ. Sci. 5 (2012) 6022, https://doi.org/10.1039/c2ee03178g.

[104] Y. Wang, R. Zhang, J. Li, L. Li, S. Lin, First-principles study on transition metal-doped anatase TiO_2, Nanoscale Res. Lett. 9 (2014) 46, https://doi.org/10.1186/1556-276X-9-46.

[105] P. Piotrkowiak, Solar Energy Conversion, Royal Society of Chemistry, Cambridge (2013), https://doi.org/10.1039/9781849735445.

[106] A. Subramanian, C.-Y. Ho, H. Wang, Investigation of various photoanode structures on dye-sensitized solar cell performance using mixed-phase TiO_2, J. Alloys Compd. 572 (2013) 11–16, https://doi.org/10.1016/j.jallcom.2013.03.171.

[107] J. Navas, C. Fernández-Lorenzo, T. Aguilar, R. Alcántara, J. Martín-Calleja, Improving open-circuit voltage in DSSCs using Cu-doped TiO_2 as a semiconductor, Phys. Status Solidi. 209 (2) (2012) 378–385.

[108] V.A. González-Verjan, B. Trujillo-Navarrete, R.M. Félix-Navarro, J.N.D. de León, J.M. Romo-Herrera, J.C. Calva-Yáñez, J.M. Hernández-Lizalde, E.A. Reynoso-Soto, Effect of TiO_2 particle and pore size on DSSC efficiency, Mater. Renew. Sustain. Energy. 9 (2020) 13, https://doi.org/10.1007/s40243-020-00173-7.

[109] T. Sakthivel, K.A. Kumar, J. Senthilselvan, K. Jagannathan, Effect of Ni dopant in TiO_2 matrix on its interfacial charge transportation and efficiency of DSSCs, J. Mater. Sci. Mater. Electron. 29 (3) (2018) 2228–2235, https://doi.org/10.1007/s10854-017-8137-2.

[110] W. Jiang, L. Yin, H. Liu, Y. Ding, Nanograss-structured counter electrode for dye-sensitized solar cells, J. Power Sources. 218 (2012) 405–411, https://doi.org/10.1016/j.jpowsour.2012.06.033.